


Review

Oxygenated Hydrocarbons from Catalytic Hydrogenation of Carbon Dioxide

Wan Nor Roslam Wan Isahak ^{1,*} , Lina Mohammed Shaker ¹  and Ahmed Al-Amiery ^{1,2} 
¹ Department of Chemical and Process Engineering, Faculty of Engineering and Built Environment, Universiti Kebangsaan Malaysia (UKM), Bangi 43000, Malaysia

² Energy and Renewable Energies Technology Center, University of Technology, Baghdad 10001, Iraq

* Correspondence: wannorroslam@ukm.edu.my; Tel.: +60-038-9216424

Abstract: Once fundamental difficulties such as active sites and selectivity are fully resolved, metal-free catalysts such as 3D graphene or carbon nanotubes (CNT) are very cost-effective substitutes for the expensive noble metals used for catalyzing CO₂. A viable method for converting environmental wastes into useful energy storage or industrial wealth, and one which also addresses the environmental and energy problems brought on by emissions of CO₂, is CO₂ hydrogenation into hydrocarbon compounds. The creation of catalytic compounds and knowledge about the reaction mechanisms have received considerable attention. Numerous variables affect the catalytic process, including metal–support interaction, metal particle sizes, and promoters. CO₂ hydrogenation into different hydrocarbon compounds like lower olefins, alcoholic composites, long-chain hydrocarbon composites, and fuels, in addition to other categories, have been explained in previous studies. With respect to catalyst design, photocatalytic activity, and the reaction mechanism, recent advances in obtaining oxygenated hydrocarbons from CO₂ processing have been made both through experiments and through density functional theory (DFT) simulations. This review highlights the progress made in the use of three-dimensional (3D) nanomaterials and their compounds and methods for their synthesis in the process of hydrogenation of CO₂. Recent advances in catalytic performance and the conversion mechanism for CO₂ hydrogenation into hydrocarbons that have been made using both experiments and DFT simulations are also discussed. The development of 3D nanomaterials and metal catalysts supported on 3D nanomaterials is important for CO₂ conversion because of their stability and the ability to continuously support the catalytic processes, in addition to the ability to reduce CO₂ directly and hydrogenate it into oxygenated hydrocarbons.

Keywords: 3D nanomaterial; carbon nanotube; graphene; catalyst; hydrocarbon; oxygenated hydrocarbon



Citation: Isahak, W.N.R.W.; Shaker, L.M.; Al-Amiery, A. Oxygenated Hydrocarbons from Catalytic Hydrogenation of Carbon Dioxide. *Catalysts* **2023**, *13*, 115. <https://doi.org/10.3390/catal13010115>

Academic Editors: Sagadevan Suresh and Is Fatimah

Received: 3 November 2022

Revised: 18 December 2022

Accepted: 19 December 2022

Published: 4 January 2023



Copyright: © 2023 by the authors. Licensee MDPI, Basel, Switzerland. This article is an open access article distributed under the terms and conditions of the Creative Commons Attribution (CC BY) license (<https://creativecommons.org/licenses/by/4.0/>).

1. Introduction

A common “Janus” type of molecule is carbon dioxide (CO₂). Several issues, including the cost of the ligand and/or the base, remain unresolved when using ecologically desirable metals to reduce CO₂. Hydrocarbons with oxygenated functional groups [1], such as carbonylic (–CO–) [2] and alcoholic (–OH) groups, are known as oxygenated hydrocarbons (Oxy-HCs). Oxy-HCR has the potential to be a cleaner, more sustainable substitute for current fossil fuels. Steam reforming of mixtures of Oxy-HCs (Oxy-HCSR) is not thought to cause a net increase in atmospheric CO₂ because Oxy-HCs derived from biological/renewable resources are thought to be CO₂ neutral. In the semiconductor, precision machining, alcohol distillery, and biodiesel industries, oxy-HCs are typically obtained as waste byproducts [3]. Hydrocarbons are the principal constituents of petroleum and natural gas. They serve as fuels and lubricants as well as raw materials for the production of plastics, fibers, rubbers, solvents, explosives, and industrial chemicals. CO₂ is a stable compound and reactions with CO₂ are thus challenging. Nevertheless, there are various reaction pathways for CO₂ hydrogenation that are dependent on the nature of the catalyst,

and a number of useful products can be obtained. Global climate change brought on by greenhouse gases has become a serious issue due to the continued use of fossil fuels, which has increased the amount of CO₂ in the atmosphere. Due to the continued increase in atmospheric CO₂ concentration (which exceeded 400 ppm in 2016), and its detrimental and potentially irreversible impact on the climate system, mitigation of CO₂ concentrations in the atmosphere is urgently needed [4]. Globally, there are plans and goals for this; the European Commission's goal is to achieve a reduction of 80–95% in greenhouse gas emissions by 2050 (compared to those of 1990) in order to achieve scientists' recommended reduction of at least 50% in global greenhouse gas emissions by 2050 [5]. China, Brazil, and Korea, among other important international partners of Europe, are tackling these problems by advancing the “low carbon economy” [6].

Currently, there are three approaches to minimize CO₂ emissions: by controlling CO₂ emissions, by capturing and storing CO₂, and by chemically converting and utilizing CO₂ [7]. Carbon storage is crucial for quickly reducing CO₂ emissions; however, it has the drawback of possible CO₂ leakage [8]. As a substitute for other carbon sources, CO₂ can be used to create feedstocks and value-added products that include carbon. In addition to providing a clean carbon supply for hydrogenation, using the CO₂ acquired through capture also helps to solve the leaking issue associated with CO₂ storage. The Sabatier reaction (CO₂ methanation) was therefore considered by the National Aeronautics and Space Administration (NASA) as a stage in recovering oxygen in closed-cycle life support systems [9]. It is possible to use even the CO₂ found in industrial exhaust gases directly as a feed for hydrogenation [10]. Therefore, it is essential and advantageous to make efficient use of renewable carbon resources in order to preserve the long-term and sustainable development of our civilization. Since CO₂ conversion needs energy input, pairing it with renewable energy would increase the sustainability and environmental friendliness of this technique. Electrocatalysis can be used to catalyze the reduction of CO₂ [11], as can photocatalysis [12] and thermal catalysis. Thermal catalysis stands out among these due to its quick kinetics and adaptable mixing of active ingredients. Being a very stable molecule, CO₂ requires energy just to be activated and then converted. The thermodynamics of the CO₂ conversion will be improved by the addition of a second material with a comparatively higher Gibbs energy. However, the fatal weakness of electrocatalysis and photocatalysis is low energy efficiency. To date, different types of metal-based electrocatalysts such as Au [13], Cu [14], Pd [15], Ag [16], Bi [17], Sn [18], and Co [19] have been intensively investigated in connection with electrochemical CO₂ reduction. Very recently, Chen et al. reported on the great importance of developing Au-based electrocatalysts with cost-effectiveness and high performance in order to commercialize CO₂ reduction technology [20]. Among the materials examined by Brouzgou et al. in 2016, reduced graphene oxide-based hybrid electrocatalysts exhibit both excellent activity and long-term stability [21]. They concluded that the development of the electrocatalyst by using materials with three-dimensional structures facilitates the electron and mass transfer process.

CO₂ is usually captured from high-concentration sources such as thermal power or chemical plants, steel mills, and cement factories. However, direct air capture (DAC) from the ambient air requires a separation unit to generate a concentrated CO₂ stream [22]. Consequently, CO₂ is hydrogenated with H₂ created using sustainable energy sources [23], and this is an exciting area of research that could yield chemicals and fuels as shown in Figure 1 [24]. CO₂ reacts over a catalyst with H₂ produced from water using renewable energy [25] to produce formic acid [26], lower olefins [27], methanol [28], and the higher alcohols [29], etc. In certain studies, the presence of H₂ was not detected, as reported by Sorcar et al. In 2019, in a study where researchers relied on natural sources, sunlight was used for a period of 6 h continuously (sustainable Joules) to recycle CO₂ into Joules-hydrocarbon fuel with a photoconversion efficiency of 1% and an efficiency of quantity estimated at 86%. The researchers reported on the use of Cu-Pt nanoparticles (Cu-Pt NPs) for the photoreduction of CO₂. From this process, methane and ethane resulted in the proportions of 3 mmol g^{−1} and 0.15 mmol g^{−1}, respectively [30]. The former problem has received

considerable attention, and researchers have already made significant strides in water electrolysis to produce H_2 using electricity produced by solar, wind, or other renewable energy sources, as well as in water splitting using photocatalytic, photo-electrochemical, or other photochemical processes. Density Functional Theory (DFT) calculations and experimental studies of the CO_2 conversion mechanism and hydrocarbon chain formation have, however, received relatively little attention in reviews to date. This review highlights the progress of research into the use of nanomaterials with three-dimensional (3D) structures and their compounds, and methods for their synthesis, in the process of the hydrogenation of CO_2 . Recent advances in catalytic performance and the conversion mechanism for CO_2 hydrogenation into hydrocarbons that have been made both through experiments and DFT simulations are also discussed. The development of 3D nanomaterials and metal catalysts supported on 3D nanomaterials is important for CO_2 conversion because of their stability and the ability to continuously support reverse transformation and Fischer–Tropsch catalysis (FT), in addition to the ability to reduce CO_2 directly and hydrogenate it into oxygenated hydrocarbons.

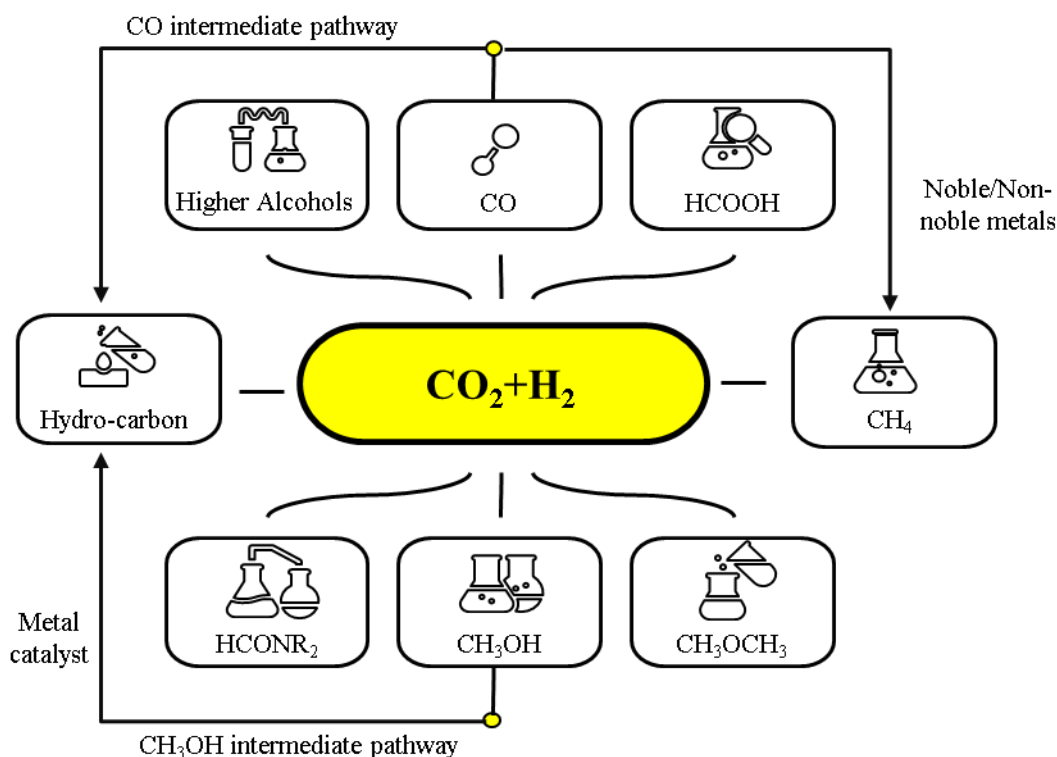


Figure 1. CO_2 to be hydrogenated to produce chemical compounds and fuels.

2. Synthesis of 3D-Structure Materials

Furthermore, different carbon or 2D-based material categories like single- or few-layer graphene are being employed for synthesizing 3D-based materials in the literature. That is, in addition to graphene, a variety of zero-, one-, and two-dimensional carbon compounds are also available, such as zero dimensional fullerene (0D) [31], 1D carbon nanotube (CNT) [32], graphene nanoribbon (GNR), carbon nanofiber (CNF) [33], and 2D transition disulfide (TMD) [34]. Due to the electrical properties being close to those of graphene, graphitic carbon nitride (g- C_3N_4) has been extensively exploited for 3D structure formation [35]. The discovery of fullerenes marked the beginning of research into carbon nanostructures (Figure 2a). The graphitization of nanodiamonds (ND) or monolithic structures of 0D materials like fullerenes or onion-like carbon are examples. 3DGMs have been created using fullerenes, which are C_{60} molecules [31]. The characteristics of C_{60} are entirely distinct from those of CNTs due to differences in size and shape. Consequently,

the 3D structure of 0D materials (C60 molecules) has various preparation techniques and potential applications. One-dimensional CNTs have been employed much more to build 3D structures than 0D fullerenes. It is interesting to note that 3D CNT aerogels were first published before 3D graphene [36]. The creation of freestanding CNT aerogels was possible after the organic fabrication of a CNT suspension with an organogelator. For instance, some organic solvents, like chloroform, can gelate single-walled CNTs (SWCNTs) modified by ferrocene-grafted poly(p-phenyleneethynylene) to create sturdy 3D CNT aerogels [32]. C60 was converted into a 3D porous carbon by potassium hydroxide activation in ammonia by Zhu et al. in their work [31]. A 3D porous carbon can be created by activating C60 powder with KOH in an Ar flow, as is briefly illustrated in Figure 2b. A 3D porous carbon that has had N added to it can be produced if the KOH activation is carried out in an NH_3 atmosphere. Pyridinic and pyrrolic nitrogen are the two kinds of doped N atoms. Meso- and macropore volume in carbon results in the desired energy storage being significantly increased by N-doping scenarios. This is actually done by the graphitization of GO and ND films, such as the mesoporous graphite film prepared by Shi et al. in 2011 [37]. GO is reduced to RGO during the graphitizing process, while ND is transformed into carbon that resembles an onion. RGO sheets were sandwiched with carbon shaped like an onion, which not only stops graphene sheets from aggregating but also creates mesopores.

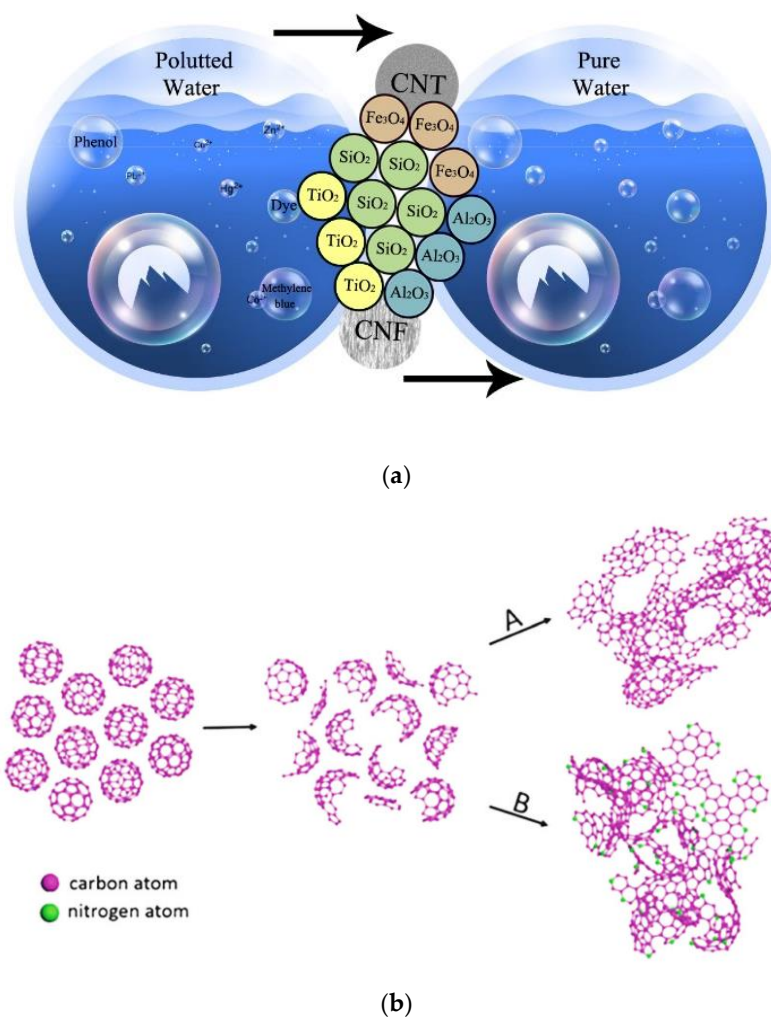


Figure 2. (a). Environmental uses of CNFs and CNTs, and (b) a diagram showing how KOH activates the C60 molecules. Route A depicts the typical activation carried out in an Ar flow, while Route B displays N-doping when NH_3 flow is involved in the activation. Reprinted with permission from Ref. [31]. Copyright © 2016, John Wiley and Sons.

Surfactants are additionally employed to disperse the CNTs and produce the aerogels. In 2007, various quantities of SWCNTs were floated in the water with sodium dodecylbenzene sulfonate (from 5–13 mg mL^{−1}) by Yodh et al. [38]. The suspensions were allowed to be converted into elastic gels overnight before being dipped into poly(vinyl alcohol) (PVA) aqueous solutions at 90 °C. Using a chemical vapor deposition (CVD) approach, Gui et al. in 2010 reported injecting a ferrocene precursor solution into dichlorobenzene to design a macroscopic and monolithic multi-walled CNT (MWCNT) sponge [39]. The fact that the diameters and the lengths of these MWCNTs varied from 30–50 nm and 10–100 mm, respectively, indicates a thick sponge of many layers of CNTs. Many CNT piles continuously stack and reach a centimeter of thickness during the growing phase of CNT sponges. The constructive vertical alignment of CNTs up from the bottom to the upper surface was a promising method to construct a 3D CNT structure without the continuous-stacking growing process. One- to three-WCNT carpets can operate well on their own, especially when they are tightly coupled to high-quality graphene.

In 2010, Zhang et al. used the CVD approach to create CNT-pillared GO and RGO platelets, for which acetonitrile was used as a carbon source and nickel as a catalyst [40]. It is possible to customize the CNTs' alignment, density, and length. A technique to create carpets of covalently bound graphene and CNTs using a floating buffer layer was revealed by Zhu et al. in 2012 [41]. In this procedure, the deposition of iron (catalyst layer) and alumina (buffer layer) was achieved to coat the graphene in sequence by electron beam (e-beam) evaporation after graphene was first produced on the Cu foil. It should also be noted that hybrid graphene–CNT ohmic-linked carpets possess a high surface area without sacrificing their standalone features [42].

In the publications cited above, CNTs can only grow on the graphene surface where catalyst particles have been deposited via dip-coating or e-beam evaporation. This, in turn, is one of the major reasons for the difficulty of producing the higher loading of active components in these graphene–CNT hybrid materials, which is crucial for electrochemical devices with high energy density. A straightforward method for creating a 3D structure made of graphene foam (GF) and CNTs was devised by Liu et al. in 2014 [43]. Therein, a hydrothermal approach was used for loading the NPs catalyst over GF. This enhanced the active component (MnO₂) loading and allowed for significantly better CNT growth on the GF than was possible with dip-coating or e-beam deposition. More recently, Jin et al. in 2016 demonstrated how a 3D current collector could make a structure of covalent carbon bonds [44]. Covalent carbon–carbon bonds bind several micrometer-long bundles of CNTs into an ultrathin GF. The coupling of e-holes in the latter composite is enabled by carbon–carbon bonds, and such bonds facilitate the charges' transportation between out circuits and electrochemically active materials.

It is important to highlight that the GNR composites created by longitudinally unzipped MWCNTs may retain their proper structure and improved electrical conductivity, which are characteristics of both CNT and graphene. An in situ unzipped approach was also realized through the CNT sponge conversion directly into GNR aerogel by Peng et al. in 2014 [45]. In this instance, the walls were opened with KMnO₄ after the oxidative chemical fluid was in-filtered into the porous sponge in order to free the walls of the nanotubes from any kind of defects. Furthermore, organic compounds like pyrrole were used by Chen et al. in 2015 as nitrogen (N) source and reagent to fabricate ultralight, highly conductive, 3D N-doped GNR aerogels [46]. GNRs are unique in that they differ from graphene sheets in having higher length/width ratio and straight edges, as well as perfect surface regularity with few flaws on the substrate. This is achieved by using GNR aerogels doped with heteroatoms to get an enhanced electronic energy-gap modulation, boosting both the reactivity of the materials and their ability in electrocatalysis when utilized as oxygen reduction reaction (ORR) catalysts. The construction of 3D carbon material types frequently involves CNFs' self-assembly into a macroscopic structure [33]. Additionally, inexpensive components like bacterial cellulose (BC) and pitch may enable large-scale production [47]. For instance, in 2014, Chen et al. worked to develop a free-standing heteroatom-doped

CNF fabrication method [48]. Initially, BC was submerged for 10 h at normal conditions in $\text{H}_3\text{PO}_4\text{-H}_3\text{BO}_3$ liquid solution. A drying step was followed by thermal treating in N_2 atmosphere for the creation of 3D carbon CNF doping heteroatoms. Furthermore, such heteroatom co-doped 3D CNFs prepared from inexpensive raw materials have outstanding energy storage performance [49]. Additionally, the template-based method has also been widely employed to create 3D CNFs [50]. Using an inexpensive melamine sponge (MS) template, Zhu et al. in 2019 produced a macroscopic 3D porous graphite C_3N_4 structure from 2D graphite C_3N_4 by one-step thermal polymerization of urea [51]. This approach is practical for the production of 3D C_3N_4 structures due to high urea loading and the light weight and good water absorbability of MS. In this instance, the produced 3D C_3N_4 samples are readily shaped by blades. Without using strong acid, Wang et al. in 2017 created C_3N_4 aerogels using an aqueous sol-gel method [52]. First, C_3N_4 NPs were produced utilizing a salt molten technique along with temperature-induced condensation of melamine using potassium thiocyanate as the solvent. The C_3N_4 hydrogels could then be produced by the C_3N_4 NP sol solution self-assembling. C_3N_4 aerogels were made using a freeze-drying process. This approach is notable because of the ability to vary the produced size and mass through the process, and its affordability, as well as the assembly without cross-linking agents.

The production and characterization of monolithic, ultra-low-density TMD (WS_2 and MoS_2) aerogels were described by Worsley et al. in 2015 [34]. Thermal degradation of freeze-dried ammonium thio-molybdate (ATM) and ammonium thio-tungstate (ATT) solutions produces the monolithic WS_2 and MoS_2 aerogels, respectively. By merely altering the initial ATM and ATT concentrations, the densities of the pure TMD aerogels may be changed to correspond to 0.4 and 0.5% of the densities of single crystals of MoS_2 and WS_2 , respectively. In 2019, Abu Zied and Alamry invented a new green synthesis method for producing 3D hierarchical $\text{Co}_3\text{O}_4\text{-C}$ NPs [53]. The extract of basil leaves (BLE) was used as a low-cost source of carbon and green template. For use as catalysts in hydrogen generation via sodium borohydride hydrolysis, various $\text{Co}_3\text{O}_4\text{-C}$ NPs have been tested. Research findings have shown both the presence of 3D porous hierarchical NPs and calcination temperature influence activity. Common features of 3D graphene, including superior mechanical strength, hierarchical porosity, large surface area, and perfect electrical conductivity, give such new materials considerable potential for applications related to catalysis, the environment, biomedicine, and most importantly, energy. Liu and Xu rapidly created a variety of 3D graphene compounds in 2019 by inventing a number of adaptable techniques [54]. The fact that graphene is a naturally occurring 2D polymer (2DP) has greatly sparked interest in the rational organic-chemical synthesis of novel 2DPs at the atomic or molecular level. The development of synthetic polymer chemistry can benefit greatly from the regulated synthesis of 2DPs with optimized molecules and superior ease of processing. Additionally, it demonstrates tremendous strength in the creation of unique polymer composites with desired characteristics and capabilities that are uncommon in traditional 1D polymers. Designing and making 2DPs that simultaneously incorporate a 2D conjugated plane, in-plane homogeneous microporosity, and electrochemically active groups is difficult yet important for the energy sector. On the other hand, due to the substantial effective surfaces, flexibility, and cycling stability, hierarchical 3D carbon nanoscale is a promising material variety for electrochemical energy applications. In order to build 3D carbon nanostructures made from carbon fibers (CFs) and electro-spun CNF (ECNFs), Alali et al. combined electrospinning with in situ CVD techniques in 2021, as illustrated in Figure 3 [55]. Ni/CNFs/ECNFs demonstrated satisfactory hydrogen evolution reaction (HER) activity in an alkaline medium with a low overpotential of 88 mV to give 10 mV cm^2 current density and Tafel slope of 170 mV dec^{-1} . This was based on the nano-nonwoven structures and forest-like growing nanostructured CNFs.

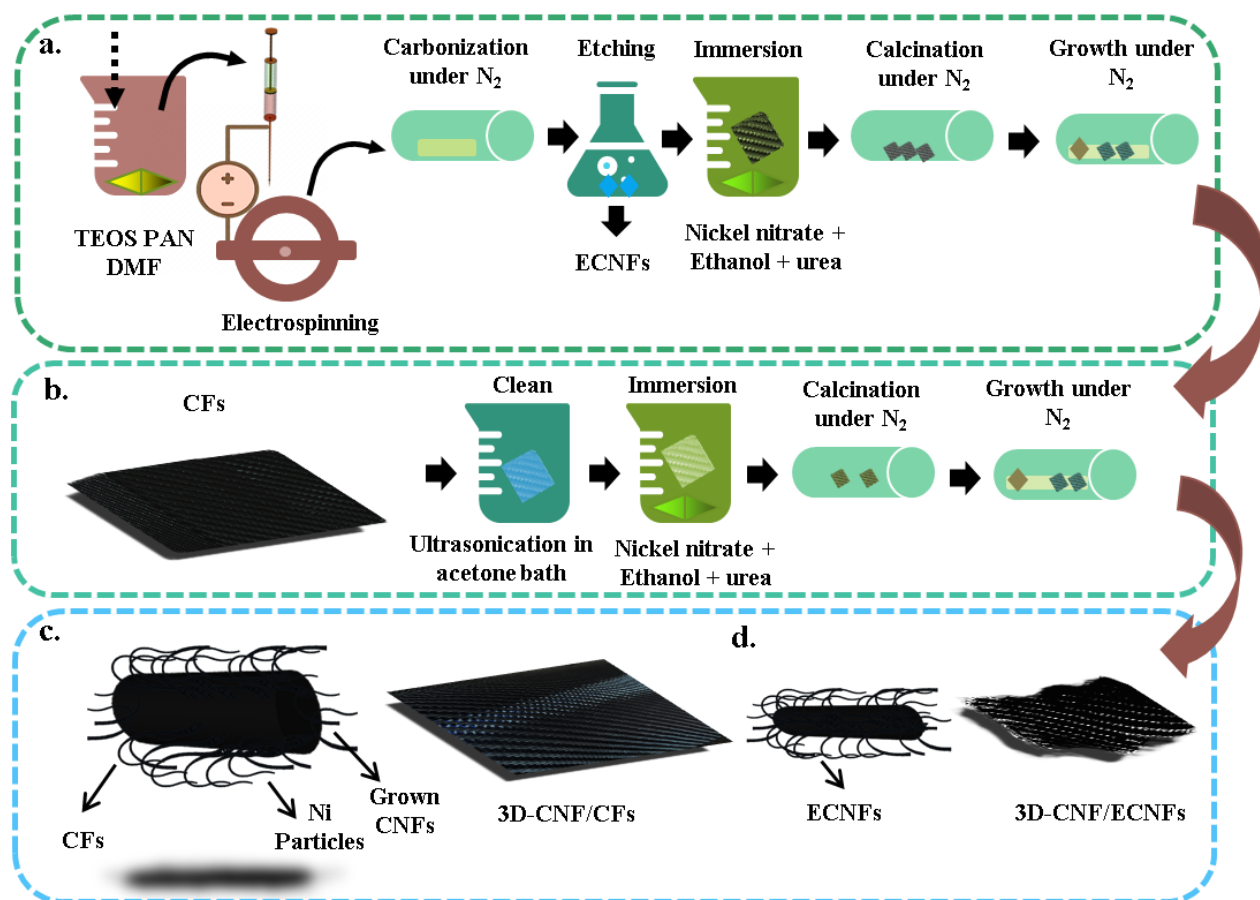


Figure 3. The steps resulting in the production of: (a) ECNFs and 3D-Ni/CNFs/ECNFs, (b) 3D-Ni/CNFs/CFs, (c) 3D-Ni/CNFs/CFs, and (d) 3D-Ni/CNFs/ECNFs. Adapted with permission from Ref. [55]. Copyright © 2021, Elsevier.

3. Graphene Production Methods

3.1. Chemical Vapor Deposition (CVD)-Based Methods

There are numerous CVD techniques that can be used today for synthesizing material compounds depending on graphene, as illustrated in Figure 4. These procedures can be categorized into seven major approaches based on the characteristics of process variables (temperature, pressure, nature of the precursor, gas flow state, deposition time, activation manner, and wall/substrate temperature) [56]. The procedures shown in Figure 5 accomplished by Arjmandi-Tash et al. in 2017 have developed the CVD-growth of graphene modalities that combine cold- and hot-wall reaction chambers [57]. Such a hybrid approach boosts growth quality to a level now comparable to other conventional CVD methods in hot-wall chambers while preserving the benefits of a cold-wall chamber, such as steady growth and high efficiency and maintaining power. Uniform monolayers of produced graphene were formed. Especially in comparison to graphene produced in cold-wall reaction chambers, charge transition experiments show a considerable increase in charge carrier mobility. Using a cold-wall CVD reactor, Alnuaimi et al. (2017) investigated the influence of graphene growth temperature and demonstrated that multilayer nucleation density is decreased under high temperatures [58]. The temperatures in that work ranged from 1000 to 1060 °C. Multilayer graphene was growing remarkably at a temperature of 1000 °C, but the nucleation rate was adversely affected at 1060 °C, so at lower growth temperatures, larger defect densities were detected. In 2019, Al-Hagri et al. created a single layer of vertically aligned graphene nano-sheet arrays (VAGNAs) with a high surface area on a Ge substrate at 625 °C using the radio frequency (RF) approach [59]. When evaluated as a

surface-enhanced Raman spectroscopy (SERS) platform, the obtained graphene demonstrated detection performance reduced to 10^{-6} M of Rhodamine 6G (R6G). By adjusting H_2 (P_{H_2}) and CH_4 (P_{CH_4}) (P_{CH_4} - P_{H_2}) partial pressure ratio, Chen et al. in 2020 created single-crystalline hexagonal bi-layer graphene (BLG) in a single step with a controlled twist angle between the layers [60].

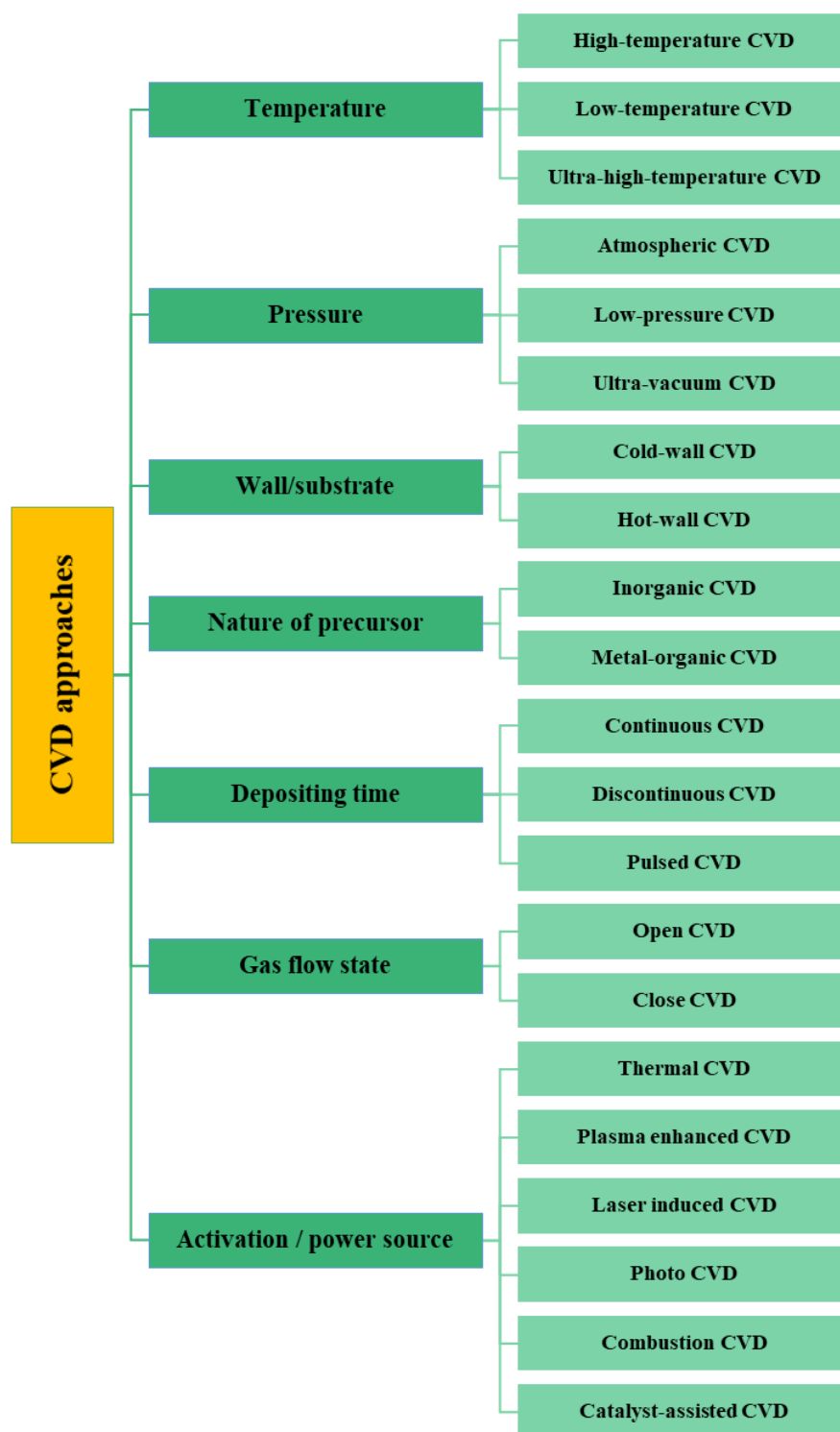


Figure 4. Summary of CVD methodologies.

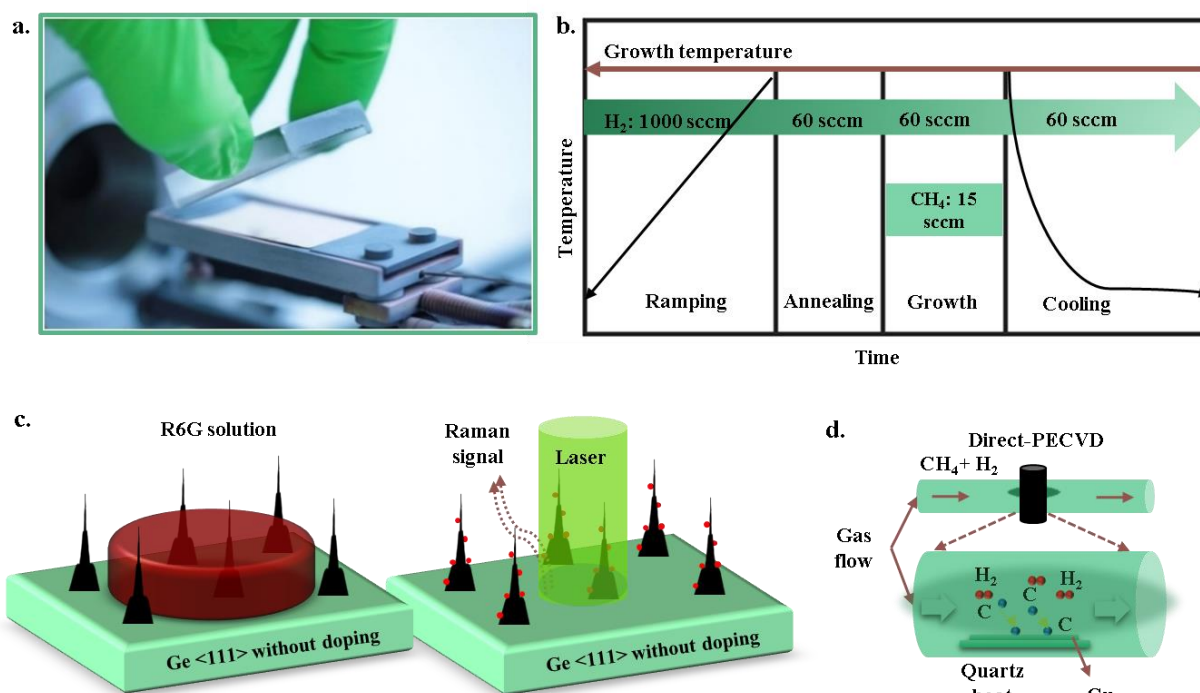


Figure 5. (a) Cold-wall chamber CVD growth of graphene. Reprinted with permission from Ref. [57]. Copyright © 2017, Elsevier. (b) The strategies that have been adopted during CVD-based graphene development. Adapted with permission from Ref. [58]. Copyright © 2017, RSC; (c) experimental process diagram, using VAGNAs as the SERS substrate. Adapted with permission from Ref. [59]. Copyright © 2022, Elsevier; and (d) production of twisted bilayer graphene with a controlled twist angle in sizes of mm and cm. Adapted with permission from Ref. [60]. Copyright © 2022, Elsevier.

3.2. Solution-Based Methods

Little if any specialist equipment is required for solution-based approaches, which assemble GO sheets onto 3D templates before chemically reducing GO to RGO (Figure 6a). In 2012, Sohn et al. succeeded in making 3D graphene capsules using spray pyrolysis with a mixture of GO-polystyrene colloidal particles [61]. An evaporation-induced capillary force was used for attaching the GO sheets to the polymer colloidal solution. The solvents used in a solution-based approach can have a significant impact on the nanostructure of the composites made of Li₂S-graphene. In 2014, Yan and his collaborators found a new methodology employing alumina fiber blanket (AFB) as a template for large-scale fabrication of microchannel-network graphene foams (mCNGFs) [62]. The procedure steps to prepare mCNGFs are depicted in Figure 6b. For effectively absorbing the GO suspension, a uniform GO solution had been used to immerse the AFB previously. AFB has a hydrophilic exterior due to the existence of hydroxyl groups on its surface. As a result, GO can readily bind to the carboxyl and hydroxyl groups on the surface of the AFB template. Additionally, capillary forces help to drive the GO to penetrate the AFB template and fill the unoccupied spaces between the alumina fibers. Following immersion in N₂ fluid, the GO-AFB composite was then freeze-dried, and the GO connected to the AFB template was converted to RGO via a thermal treatment under nitrogen atmosphere at 500 °C. Finally, HF was used to remove the AFB template to acquire the pure mCNGFs. In 2018, Shunxin et al. reported that anhydrous N-methylpyrrolidone (NMP) has excellent wettability characteristics with graphene and its functional groups have higher energies with Li₂S. NMP solvent was utilized in that study for Li₂S-graphene composite preparation [63]. The researchers claimed that the graphene surface had a good amount of uniformly distributed nano-Li₂S. Apparently, nano-Li₂S presence reduces the p-p interactions between graphene sheets, and the composite of Li₂S-graphene displays a honeycomb-like structures with a majority of micropores. The Li₂S-graphene composite showed better electrochemical

performance in terms of high columbic efficiency, low potential barrier, highly energetic capacity, and a high-rate capability.

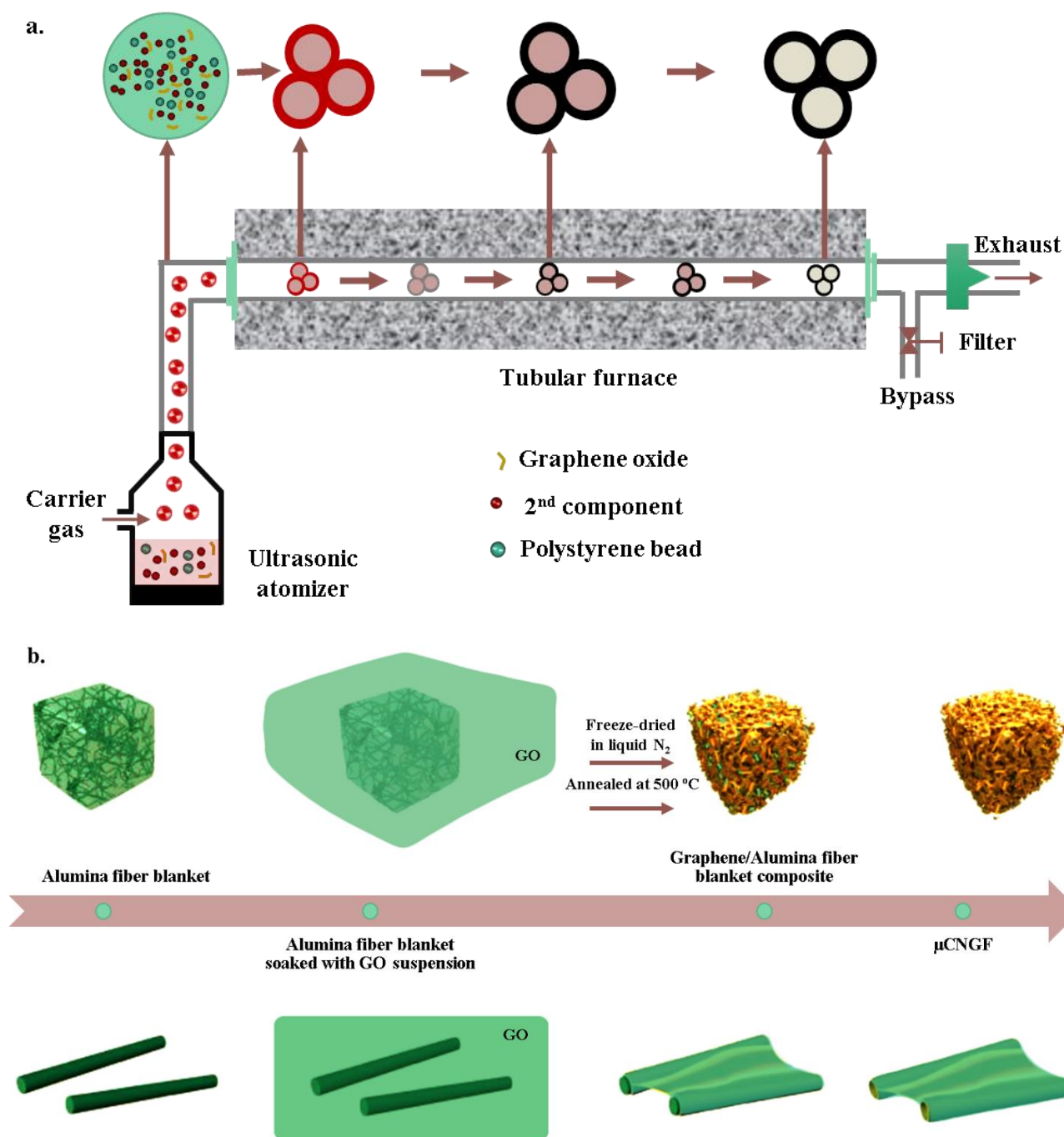


Figure 6. (a) rGO capsule production experimentally. Adapted with permission from Ref. [61]. Copyright © 2012, Royal Society of Chemistry. (b) The procedures involved in producing mCNGFs. Adapted with permission from Ref. [62]. Copyright © 2014, Royal Society of Chemistry.

3.3. Three-Dimensional (3D) Printing

An efficient and simple methodology to facilitate direct fabrication of 3D bulk objects is 3D printing. [64]. By carefully casting Ni and sucrose mixture onto a substrate, Sha et al. in 2017 reported the effective development of an automated metal powder 3D-printing approach for in situ synthesis of free-standing 3D GFs. They then used a commercial CO₂ laser to transform the Ni-sucrose mixture into 3D GFs, as clearly shown in Figure 7a [65].

This technology permits direct in situ 3D printing of GFs without the need for a rising furnace temperature or an extended growing phase. It blends powder metallurgy templating with 3D-printing techniques. The 3D-printed GFs exhibit multilayer, low density (0.015 g cm^{-3}), high quality, and high porosity rate (99.3%) for graphene characteristics. The GFs have an impressive storage modulus of 11 kPa, an electrical conductivity of 8.7 S cm^{-1} , and a high damping capacity of 0.06. By developing hybrid inks and printing schemes to enable mixed-dimensional hybrid printability, Tang et al. (2018) proposed a generalized 3D-printing methodology for graphene aerogels and graphene-based mixed-dimensional hybrid aerogels with complex architectures, overcoming the limitations of multicomponent inhomogeneity and harsh post-treatments for additives removal (Figure 7b) [66]. The 3D-printed hybrid aerogels were also shown to act as ultrathick electrodes in a micro-supercapacitor that could withstand symmetrical compression while still demonstrating quasi-proportionally improved areal capacitances under heavy mass loading. The strong ion- and electron-transition routes offered by the 3D-printed, densely linked networks were responsible for the remarkable performance.

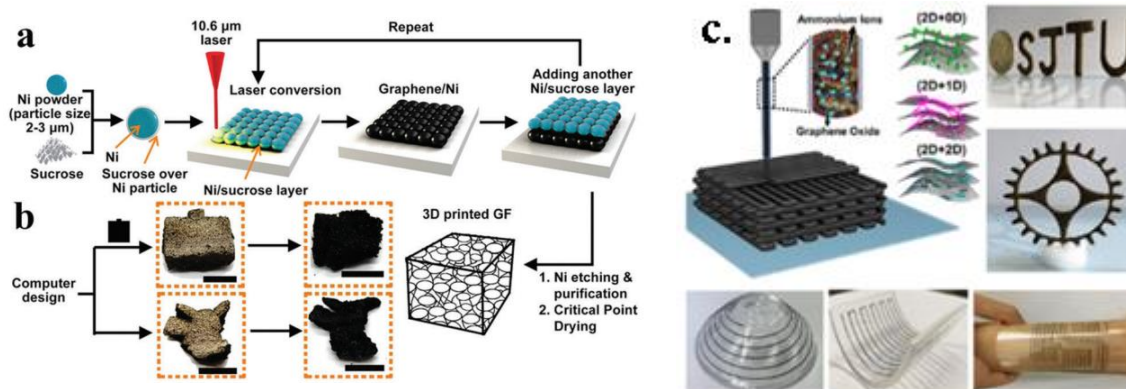


Figure 7. (a) Diagram of an in situ 3D GF synthesis method that simulates 3D printing. Reprinted with permission from Ref. [65]. Copyright © 2017, American Chemical Society, (b) images of 3D-printed GF taken before and after the Ni was dissolved. Reprinted with permission from Ref. [65]. Copyright © 2017, American Chemical Society. (c) Mixed-dimensional hybrid aerogels based on graphene. Reprinted with permission from Ref. [66]. Copyright © 2018, American Chemical Society.

3.4. Hydrothermal Method

Hydrothermal process flexibility increases the possibility of doping the graphene lattice with nitrogen or boron, for example, to prepare better quality 3DGMs. Specific additives, such as swelling and cross-linking agents, can be added to the GO dispersion forming these 3DGMs [67]. To produce extremely effective graphene–metal oxide-based hybrid supercapacitors, Bai et al. proposed in situ synthesis of 3D-graphene-MnO₂ foam composite in 2020 [68]. The 3D graphene-MnO₂ composite underwent in situ conformal development and exhibited excellent crystalline nature and low contact resistance, which increased the electrolyte performance at transporting charges. Relatively, the 3D conductive graphene foam allowed electrolyte ions to migrate across the MnO₂ surface quickly because of its porosity. In the supercapacitors, the 3D graphene-MnO₂ composite electrode demonstrated high specific capacitance (333.4 F g^{-1} at 0.2 A g^{-1}) and remarkable cycle stability in the absence of carbon black. This scientific method for creating a composite made of 3D graphene and MnO₂ offers a potential method for producing energy storage electrode materials to design high-performance supercapacitor devices. Pure 3D graphene is regarded as a suitable platform to load catalytic components, including metals, due to its low density, excellent electrical conductivity, exquisite flexibility, and high surface area [69], metal oxides [70], and metal sulfides [71]. In fact, using hydrothermal techniques, inorganic nanomaterials can grow in situ on the surface of 3D graphene.

3.5. In Situ Chemical Reduction

A 3D graphene architecture can be created using in situ self-assembling graphene fabricated by mild chemical reduction. The pore size, electrical conductivity, mechanical strength, and density of the 3D graphene preparation are all significantly affected by the choice of reducing agent. Different types of reducing agents have been studied, including hydrazine hydrate [72], metals [73], metal hydrides [73], phenolic compounds [74], and reduced sugars [75]. In 2011, Chen et al. created 3D graphene from a homogenous dispersion of Fe_3O_4 NPs in GO aqueous suspension. Additionally, they produced a 3D magnetic graphene- Fe_3O_4 aerogel during the reduction of GO to graphene [76]. This offers a useful approach for preparing 3D graphene-NP composites for a variety of uses, such as energy conversion and catalysis. For a superior and reasonably priced electro-catalyst, Kabtamu et al. reported a 3D annealed tungsten trioxide nanowire-graphene sheet (3D annealed WO_3 NWs/GS) foam in 2017 [77]. It was produced using in situ self-assembling graphene sheets that were prepared by mild chemical reduction, then freeze-dried, and finally annealed using vanadium redox flow battery (VRFB) electrodes (Figure 8). A 3D annealed WO_3 NWs/GS foam exhibited the desired electrocatalytic activity toward V^{2+} - V^{3+} and VO^{2+} - VO^{2+} redox couples. Charge-discharge tests further demonstrated that the 3D annealed WO_3 NWs/GS foam used in a single flow cell of a VRFB exhibited excellent energy efficiencies of 79.49 and 83.73% at current densities of 80 mA cm^{-2} and 40 mA cm^{-2} , respectively. These energy efficiencies are significantly higher than those of cells assembled with pristine graphite felt and 3D WO_3 NWs/GS foam with no specific heating process. It also does not appear to have degraded after 50 charge-discharge cycles. Such findings indicate that every WO_3 NW sample is firmly anchored to the GS and are essential for aiding the redox reactions of the vanadium redox couples, are attributable to the production of new W-O-C bonds. Additionally, WO_3 NWs/GS foam confirms the VRFBs electrochemical performance according to its 3D hierarchical porous structure after annealing, as is illustrated in Figure 8.

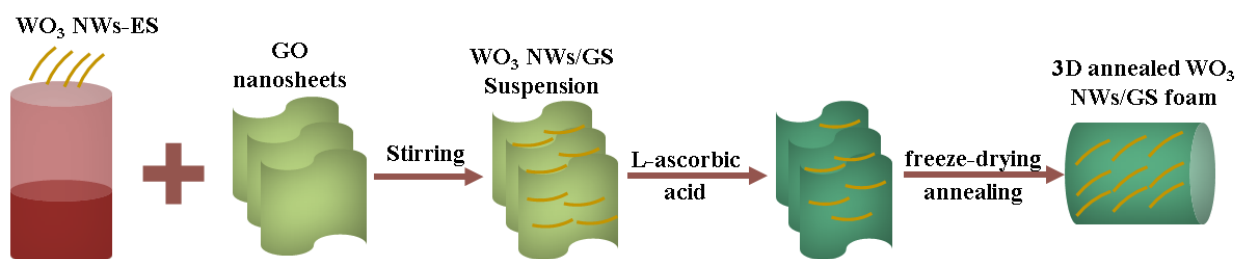


Figure 8. Graphical representation of 3D annealed WO_3 NWs-GS foam preparation. Adapted from Ref. [77]. Copyright © 2017, Royal Society of Chemistry.

3.6. Pyrolysis of Organic Precursors

Pyrolysis of organic precursor materials such as glucose [78], resorcinol-formaldehyde [79], phenol-furfural [80], and chitosan [81], is a quick and efficient way to manufacture 3DGMs on a large scale. A 3D porous graphite carbon was created by pyrolyzing a conjugated polymeric molecular precursor framework, according to To et al. in 2015 [82]. The obtained 3D porous graphite carbon had a record-high surface area ($4073 \text{ m}^2 \text{ g}^{-1}$), a sizable high porosity (2.26 cm^3), and outstanding electrical conductivity (300 S m^{-1}).

4. Uses of Graphene as a Catalyst

One of the carbon allotropes is called graphene, and it is composed of hexagons. Among the several elements of the carbon family, the use of graphene—a 2D single hexagonal carbon sheet—is on the rise. Ever since the first manufacture of it was announced in 2004, the scientific and technical sectors have examined graphene in great detail [83]. Fullerene (0D), nanotube (1D), and graphite (3D) are some other allotropes, as seen in Figure 9. Reduced GO, graphene quantum dots, and GO are examples of graphene-based nanomaterials.

rials. Although some components of the graphene family have sp^2 and sp^3 carbon atoms instead of the ideal sp^2 carbon atoms, this is because functional groups including hydroxyl group, carbonyl group, carboxyl group, and epoxy group have been added. GO, which is a single layer of graphite oxide, is typically created chemically by oxidizing graphite [84]. GO containing oxygen includes a variety of functional groups, as seen in Figure 9. With the exception of a small quantity of carbonyl, carboxyl, phenols, lactone, and quinones groups at the sheet's borders, these functional groups are primarily hydroxyl and epoxide groups in the basal planes [85]. GO possesses a wide variety of functional groups at its edges and basal planes, which enables it to be functionalized and exfoliated to produce well-dispersed fluids on distinct GO sheets in polar and non-polar fluids. As a result, it has many different applications, including nanocomposites [86], photocatalytic degradation [87], batteries [88], condensers [89], and sensors [90].

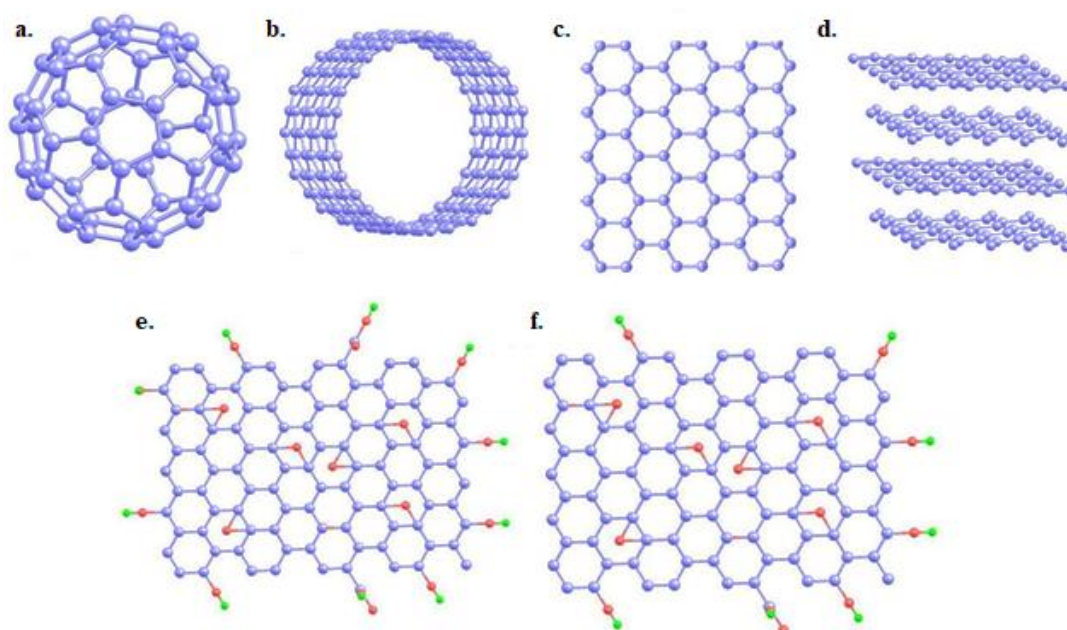


Figure 9. (a) 0D Fullerene, (b) 1D CNT, (c) 2D graphene, (d) 3D graphite structures, (e) GO, and (f) reduced GO (light purple—carbon; red—oxygen; and green—hydrogen).

Geim et al. isolated a single-graphite nanosheet layer in 2004 using a scotch tape peeling approach [91]. Because of the mentioned special characteristics in relation to chemical reactions, physical science, materials science, and mechanical applications, graphene and its compounds have received considerable attention ever since this significant advance. For example, graphene has a remarkable specific surface area of $2630 \text{ m}^2 \text{ g}^{-1}$, $10,000 \text{ cm}^2 \text{ V}^{-1} \text{ s}^{-1}$ carrier mobility, 5000 W m K^{-1} thermal conductivity at ambient temperatures, 97% optical transparency, strong chemical stability, and high mechanical strength with a 1.0 TPa Young's modulus [92].

Several synthesis techniques like CVD [93], physical exfoliation approach [94], graphitization, and chemical oxidizing cleavages [92], have been used for the purpose of 2D materials fabrication. Research on graphene in the areas of life sciences, energy applications, and environmental monitoring has advanced significantly as a result of simple techniques for graphene synthesis. Graphene is a versatile 2D building block that has been put together to form 1D fibers [95], 2D films [96], and 3D aerogels or hydrogels [97], all of which significantly broaden the scope of graphene applications and upcoming specific products. Due to the ability of 3D graphene to preserve the original properties of the material in the 2D phase, there have been extensive studies on the design and development of 3D graphene by assembling it from 2D graphene [65]. Based on these exciting characteristics, 3D graphene has indeed met some of the prerequisites to be regarded as an

advanced catalyst or as a catalytic support. Meso-, micro-, and macropores are combined in 3D graphene-based materials (3DGMs) in such a way that the micro- and mesoporosity provide them with a high specific surface area while the macroporosity ensures accessibility to this surface, which is more advantageous for improving catalysis efficiency. It is important to remember that the confinement effect of catalytic elements within 3D graphene can stabilize effective regions through catalyzed reaction [98]. A distinctive benefit of these 3DGM monoliths is their integrated structure, thus making it simple to manipulate and collect when in use and eliminating any potential ecological concern brought on by the discharge of harmful graphene nanosheets [99]. The main functions and advantages of using 3DGM are illustrated in Figures 10 and 11, respectively. Numerous 3DGMs made of 2D materials with various distinct morphologies have been successfully produced and used as a result of the rapidly developing production approaches and evaluation procedures. Significantly, these 3DGMs have also been proven to perform admirably within catalyst regions. In addition to surface area, it is clear that the monolith contact angle will dictate how easily they can access electrolytes, which will ultimately impact the effectiveness of their catalysts. 3DGMs are stronger catalysts than 2DGMs because of their superior wettability. In catalytic reactions, 3DGMs appear to provide more benefits over 2DGMs. Unpolluted water shortages are a problem worldwide due to the rising demand for unpolluted water resources brought on by the rapid rise of industrialization, rising pollution emissions, and protracted droughts [100]. As a result, numerous approaches and solutions have been used to increase the amount of water resources that are readily available [101]. Long-term reusing of rural or municipal wastewater from treatment plants originating from agricultural and industrial operations can be accomplished with the use of chemical processes. Advanced oxidation processes (AOPs) are a category of water purification techniques based on the in situ generation of highly active transient species, like the reagents O_2 and OH ; such reagents help in mineralizing the organics and disinfecting the harmful microorganisms in wastewater. Due to their potential to provide low-cost and extremely efficient platforms, photocatalytic techniques using semiconductor devices have been in the forefront of AOPs [102]. Using the hydrothermal approach, Qiu et al. (2014) embedded TiO_2 nanocrystals into high-porosity graphene aerogels (TiO_2 -GAs) [103]. Substantial quantities of organic pollutants can be absorbed by TiO_2 -GAs due to their higher surface area and hierarchical channel structures. Additionally, TiO_2 -GA electron transmission facilitation and electrical conductivity can be improved by the addition of high conductivity GAs to the TiO_2 matrix. The researchers exploited this composite's excellent photocatalytic activity and its long-term stability for methyl orange (MO) degradation. The synergistic interfacial connections between TiO_2 nanocrystals and GAs, high conductivity, faceted features, and high elasticity were credited for these positive effects. Individual TiO_2 -GA composites are considerably easier to separate from the liquid reaction medium due to their large dimensions, and they can be separated with just a pair of hand tweezers. According to Fan et al. in 2015, AgBr-GA composite is able to photoreduce CrVI and photooxidatively degrade MO [104]. As per the researchers, AgBr-Gas photocatalytic capability and observed stability resulted in the preservation of the AgBr-GAs quality and morphology even after numerous photocatalytic cycles (only 0.8% losses were reached after carrying out all the degradation cycles). In some traditional catalytic reactions, such as hydrolysis of ethyl acetate, the high mass transfer resistance in 3DGMs hinders the catalytic performance as compared to the 2D graphene. Although the defects from the formation process of 3D structure are favorable to some catalytic reactions, they lead to a reduction in the electrical conductivity of 3DGMs as compared to 2DGMs. The figures below list each function with its structural benefits, and also the advantages of 3DGMs in catalysis.

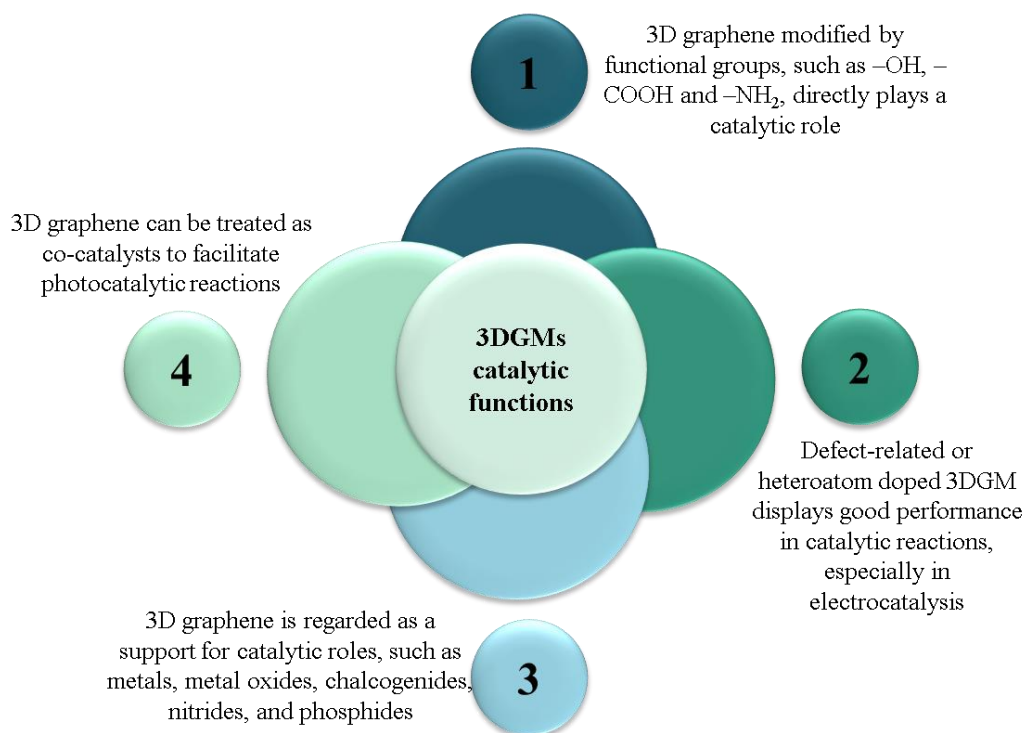


Figure 10. The main functions of 3DGMs in catalysis applications.

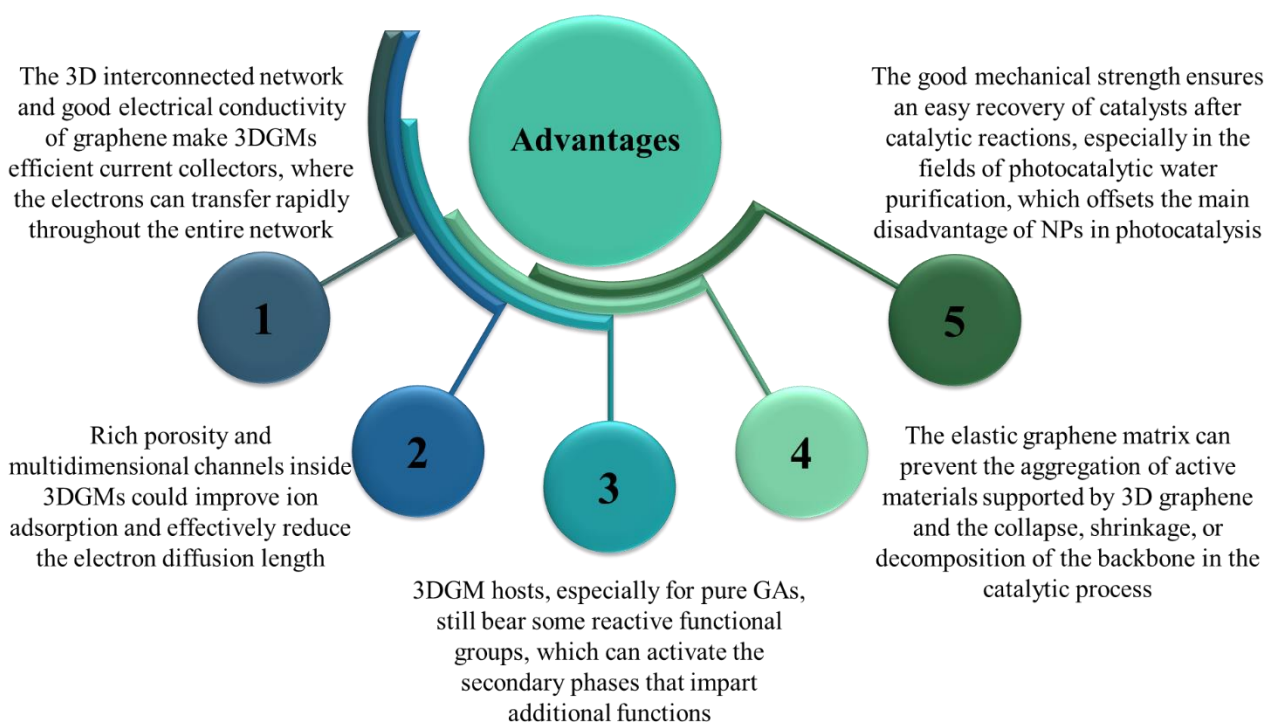


Figure 11. The main advantages of using 3DGMs in catalysis applications.

5. CNT Production Methods

Several methods in the literature have been developed to produce large quantities of CNTs via process gases or vacuum. In Figure 12, arc discharge, laser ablation, high-pressure carbon monoxide disproportionation, and chemical vapor deposition (CVD) are shown [33].

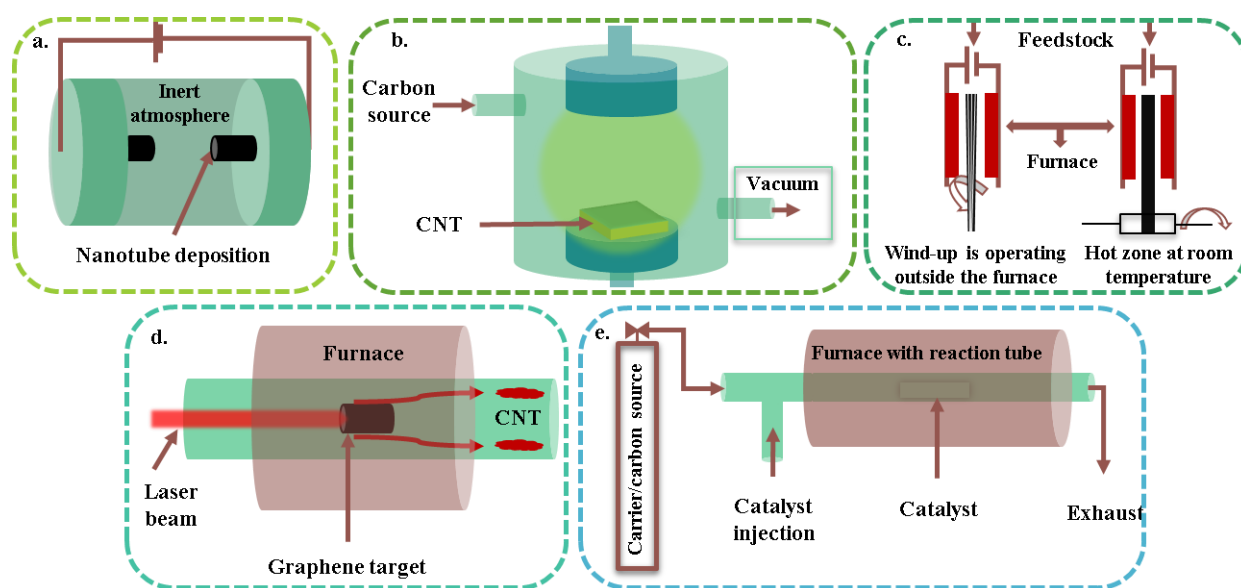


Figure 12. Various schematics for CNT fabrication techniques: (a) arc discharge apparatus, (b) parallel plate PECVD system, (c) direct aerosol spinning process, (d) laser ablation method, (e) thermal CVD system with a tube furnace.

5.1. Arc Discharge

In 1991, Iijima presented the creation of a novel class of finite carbon structures made of needle-like tubes [105]. Identical to how fullerene is made, the tubes were made utilizing an arc discharge evaporation process. The carbon electrode utilized for the direct current (dc) arc-discharge evaporation of carbon in a vessel filled with argon at a pressure of around 100 Torr was used to develop the carbon needles, which ranged in size from 4 to 30 nm in diameter and up to 1 mm in length. This process yielded both single-walled and multi-walled nanotubes with lengths of up to 50 μm and minimal structural flaws, with up to a 30% weight yield. Higher temperatures (over 1700 $^{\circ}\text{C}$) are used in the arc-discharge method for CNT synthesis, which often results in expansion of CNTs with fewer structural flaws [106]. In another study, SWCNTs were produced by Zhao et al. in 2019 utilizing a modified arc-discharge furnace with buffer gas of 500 Torr helium at 600 $^{\circ}\text{C}$ [107]. Transmission electron microscopy (TEM), X-ray diffraction (XRD), and Raman spectroscopy were used to investigate the impact of the catalyst type on the generation of the SWCNTs. According to the research observations, the catalytic structure had a significant effect on the rate and purity of the final SWCNTs produced. At a catalyst loading of 3 wt%, Fe-Ni-Mg and Co-Ni powder catalysts displayed superior photocatalytic activity. The mean diameter of the SWCNTs was about 1.3 nm, and the soot production rate could reach 15 g/hr. Regarding the electrical energy storage and conversion devices application, Tepale-Cortés et al. in 2021 used the arc-discharge method to synthesize the required CNT structure by vaporizing the graphite rods while using Ni and a Ni/Y combination as catalysts. [108]. In a cylindrical glass reactor with a regulated Argon flow rate of 1.43 $\text{cm}^3 \text{min}^{-1}$ and a chamber pressure of 39 kPa, CNTs were produced. Carbon powder had been gathered first from the reactor following chemical treatment with HCl solution at 1 M for metallic contaminants removal. SEM and TEM morphological characteristics revealed that MWCNTs have amorphous carbon particles stuck to their surfaces. FT-IR spectra showed bands at 1550 and 1200 cm^{-1} that corresponded to C=C bonds specific to CNT skeletons which were absent in the pristine graphite. UV-Vis was used to detect electromagnetic absorption, with peaks at 204 and 256 nm being associated with MWCNTs' sp^2 hybridization property.

5.2. Laser Ablation

Richard Smalley et al. in 1996 used a laser ablation method to vaporize graphite rods with a tiny quantity of cobalt and nickel at 1200 °C, yielding >70% high yields of SWNT [109]. The laser ablation technique requires bleeding an inert gas into a chamber, and laser pulses of pulsed-laser type supply a higher temperature for graphite evaporation. As the evaporated carbon particles condense on the reactor cooler surface, nanotubes will be developed there. A water-cooled surface should be used in the setup for collecting nanotubes. The tubes grow up until an excessive number of catalytic atoms accumulate at the nanotube end. The yield of the laser ablation approach is about 70% and it predominantly yields SWCNTs of a controlled size dictated by the reaction temperature. However, it costs much more than the CVD or arc-discharge methods. In 2017, Khashan et al. studied the antibacterial property of iron oxide NP-decorated CNTs that had been effectively created using liquid laser ablation with Nd:YAG pulses [110]. The composite NPs were observed using TEM, which revealed semi-spherical iron oxide NPs that were aggregated around rolled and unrolled graphene sheets. The existence of carbon and other iron oxide NP phases was demonstrated by the XRD spectra. Then, utilizing iron oxide-enhanced nutritional broth and nutrient agar procedures, the NPs' antibacterial activity was evaluated against various bacteria. Wu et al. in 2019 accomplished a patterning and ablation of CNT film using a femtosecond laser with various parameters [111]. Investigating the effects of laser pulse energy and pulse number on ablation holes led to the discovery of a 25 mJ/cm² ablation threshold. The pattern behavior groove was evaluated using Raman spectroscopy and SEM analysis. The outcomes demonstrated that the laser ablation removed the oligomer from the CNT film, which increased the Raman G band intensity. Once the pulse's energy was able to break the C-C bonds between distinct carbon atoms, the CNTs' ablation was brought about by the interaction of photon energy with laser-induced thermal elasticity. During laser cutting at higher energy, contaminants including amorphous carbon were discovered at and around the cut edge, and significant distortion and tensile stress formed on the CNT groove. In order to adorn CNTs with various concentrations of ZnO NPs on their tubular surface in only one step for catalytic degradation against methylene blue dye, Mostafa et al. in 2021 used the laser ablation procedure in liquid media [112]. By maximizing the laser ablation period, the number of decorated ZnO NPs was kept under control. The nanocomposite's structure was investigated using a variety of techniques, including optical, structural, and morphological analyses, which revealed that the interaction between ZnO and the CNTs had a different impact on the absorbance characteristic peak. It has been observed that if the ablation duration increased, the amount of ZnO coating on the CNTs increased. The researchers in this work demonstrated that the CNTs' presence in the composite significantly increased the photocatalytic performance when compared to pure ZnO.

5.3. Chemical Vapor Deposition (CVD)

Probably the most popular technique for creating CNTs is CVD [113]. A layer of metal catalyst particles, such as nickel, cobalt iron, or a mixture, is produced on a substrate during the CVD technique. Oxide reduction and oxide solid solutions are other methods for making metal NPs. The sizes of the metal NPs from which the nanotubes are to be generated will vary [114]. An annealed metal layer, patterned metal deposition, or plasma etching of a metal layer can all be used to manage this. In the CVD process, the reaction chamber is filled with a mixture of hydrocarbon gas, such as acetylene, methane, or ethylene, and nitrogen. When the hydrocarbons break down throughout the reaction at temperatures ranging from 700–900 °C and air pressure, nanotubes are constructed on the substrate. The direction of the electric field will be followed by the growing nanotube if a strong electric field is applied (plasma-enhanced CVD). Due to its low cost per unit and ability to produce nanotubes directly on a specified substrate, CVD holds the greatest promise for industrial-scale deposition [115]. The development of CNTs from liquefied petroleum gas (LPG) on a Fe₂O₃-Al₂O₃ precatalytic by using CVD procedure without hydrogen was

reported by Duc et al. in 2019. The resulting MWCNTs had identical external tube diameters of 50 nm, but they had a less imperfect construction. The $\text{Fe}_2\text{O}_3\text{-Al}_2\text{O}_3$ precatalytic had been reduced to $\text{Fe-Al}_2\text{O}_3$ during the synthesis process utilizing the byproducts of LPG breakdown, according to the CNTs' growth mechanism, and a tip-growing process was proposed. The resulting CNTs were employed to adsorb the copper from liquids after being surface-modified with potassium permanganate in the acid medium. The adsorption data were evaluated using the Freundlich and Langmuir isotherm models, and the maximum adsorption capacity of Cu(II) was 163.7 mg g^{-1} [116]. First principles nonequilibrium quantum chemical molecular dynamics simulations of the breakdown of ferrocene (Fc) during floating catalyst CVD (FCCVD) were described by Mclean et al. in 2021 [117]. The key growth agents for the nucleation of carbon chains from Fc-derived species like cyclopentadienyl rings are produced when these species are dissociated into C_2H_x radicals and C atoms, according to their analysis of the effects of additional growth precursors like ethylene, methane, CO, and CO_2 on the Fc decomposition method. Without the need for an extra growth precursor, Fc degrades due to the spontaneous cleavage of the Fe-C and C-H bonds, allowing for the clustering of Fe atoms to create the floating catalysts. They described the two competing chemical routes that were present during the earliest stages of FCCVD—the growth of Fe NPs catalysts and the growth of carbonic chains—on the basis of these simulations. The latter can be facilitated in the presence of additional growth precursors, with the type of precursor dictating how these conflicting pathways are balanced. The latest CVD development of SWNTs from plastic polymers, such as low-density polyethylene (LDPE) and polypropylene (PP), was presented by Zhao et al. in 2022 [118]. Successfully developed cobalt catalysts supported by porous magnesia (Co-MgO), the porosity of which restricts the mobility of reduced Co NPs and facilitates the nucleation of small diameter SWNTs, was credited with the successful synthesis of SWNTs from the polymers. The method was also expanded to catalyze the creation of SWNTs from waste plastics such as food packaging film and melt-blown mask filters. This proof-of-concept development shows the potential of using plastic pollution as a feedstock to create valuable carbon nanomaterials.

5.4. Plasma Torch

A thermal plasma technique can also be used to create SWCNTs [119]. More CNTs can be continuously created using the plasma torch process. Since 2001, a number of academic institutions have studied how to make CNTs in plasma jet reactors using this method [120]. The procedure is inexpensive and ongoing. The atmospheric pressure plasma in a microwave's plasma torch, which takes the shape of an intense "flame", atomizes a gaseous combination of ethylene and argon. SWNT, metallic, and carbon NPs, as well as amorphous carbon, are all present in the flame's emissions. Using an induction thermal plasma technique with a plasma torch is another way to make SWCNTs. SWCNTs with various diameter distributions can be created. With this process, it is possible to manufacture two grammes of nanotube material each minute, which is more than with arc discharge or laser ablation [121]. An electron-rich poly(fluorene-co-carbazole) derivative is used to extract semiconducting species from the initial HiPCO or plasma-torch nanotube starting material, and then an electron-poor methylated poly(fluorene-co-pyridine) polymer is used to isolate the metallic species that are still present in the residue. Bodnaryk et al. reported this two-polymer system in 2018 [122]. The metallic species in the sample were two times more enriched using this process than they were from the raw starting material. These findings suggest that an efficient method for enriching metallic species is the use of polymers with low electron density. Assa et al. combined regioregular poly(3-hexylthiophene) (P3HT), 1-(3-methoxycarbonyl) propyl-1-phenyl[6,6]C61 (PCBM), and torch-plasma-grown SWCNTs as a hybrid photoactive layer for bulk heterojunction solar cell devices in 2019 [123]. Investigators showed that even when sputtering is done using a Cs^+ 2000 eV ion source, chemical information can be properly acquired by time-of-flight secondary ion mass spectrometry throughout the hybrid organic photoactive solar cell

layers. The highest results were attained with 0.5 wt% SWCNT loads, resulting in a power conversion efficiency of 3.54% and an open-circuit voltage (VOC) of 660 mV. To better understand the charge-transfer mechanisms occurring at the P3HT:PCBM:SWCNT interfaces, J_{sc} was measured with respect to light intensity and exhibited a linear dependency (in the double logarithmic scale). This suggests that monomolecular recombination is more likely to be responsible for charge carrier losses at this optimal SWCNT concentration of 0.5 wt%. Finally, they reported that hybrid devices are able to significantly increase the exciton dissociation efficiency thanks to the fullerene's electron-accepting nature and the SWCNT's fast electron transit feature. In 2021, Gotthardt et al. demonstrated that 1,2,4,5-tetrakis(tetram-ethylguanidino)benzene (TTMGB), a guanidino-functionalized aromatic compound, is a successful n-dopant for field-effect transistors (FETs) with gold contacts and networks of semiconducting SWCNTs with small diameters and large band gaps [124]. After TTMGB treatment, the work functions of gold, palladium, and platinum were found to have decreased by about 1 eV, according to Kelvin probe measurements. In turn, gated four-point probe measurements revealed orders of magnitude lower contact resistances for electron injection into SWCNT networks. TTMGB treatment did not affect the electron transport or maximum mobilities in SWCNT networks at high carrier densities, according to measurement techniques that were temperature- and carrier concentration-dependent, but it significantly increased the subthreshold slope of nanotube FETs by removing shallow electron trap states.

6. Uses of CNT as a Catalyst

A variety of carbon bonds work to construct a new different structure of unique features. A layered structure with a weak out-of-plane van der Waals bond can be built by sp^2 hybridized carbon. The strong in-plane bonds play a major role in this purpose. A few to a few tens of concentric cylinders with regular periodic interlayer spacing locate around ordinary central hollow and made MWCNTs. The real-space analysis of multiwall nanotube images has shown a range of interlayer spacing (0.34 to 0.39 nm) [125]. It was discovered that CNTs had superior thermal transfer properties. For instance, it was discovered that CNTs had extraordinarily high axial thermal conductivities, around 2000 W/mK or more than 3000 W/mK for MWCNTs, and much higher for SWCNTs [126], and it was found that CNT-in-polymer and CNT-in-oil suspensions had massively enhanced thermal conductivity. Even the short CNTs agglomeration, randomly entangled with one another, have been employed in earlier studies [127]. Then, on ceramic spheres, large-scale CNT arrays with millimeter vertical alignment have been constructed [128]. High-speed shearing can easily spread them into fluffy CNTs. CNTs also demonstrated incredible catalytic uses [129]. Long CNTs (over 500 m) intercrossed Cu/Zn/Al/Zr catalyst (CD703) were produced in 2010 by dispersing CNT arrays of vertical alignment in Na_2CO_3 fluid and co-precipitating with metal nitrite. When comparing Cu/Zn/Al/Zr catalytic compound without CNTs, the space time yield (STY) of methanol on CD703 rose by 7 and 8%, respectively, to 0.94 and 0.28 g/(g_{cat} h) for CO and CO₂ hydrogenation. Additionally, dimethyl ether (DME) has been formed by one step CO and CO₂ hydrogenation with a STY of 0.90 and 0.077 g/(g_{cat} h) at 270 °C when paired with γ -Al₂O₃ catalyst and HZSM-5. A CD703 catalyst exhibited great action with production of methanol as a result of phase separation, ions dopant, valence compensating, hydrogen reversibly adsorbent and storage on CNTs promoting hydrogen spillover. Since CNTs have higher thermal conductivity, CD703 has better stability. It was thus revealed that using Cu/Zn/Al/Zr catalytic compounds for the synthesis of methanol and DME from CO/CO₂ hydrogenation was well-promoted by long CNTs [130]. Typically, bulk linked CNT constructions are used in the aerospace, automotive, robust electronics, and biomedical industries and have interesting properties [131]. It is still difficult to join CNTs at interconnects to form effective 3D constructions with a desired strength [132]. Spark plasma sintering (SPS) has been used under a range of pressure and temperature settings to synthesize bulk CNT linked structures. The interconnected 3D structures and the impact of processing conditions on structural damage to CNTs were examined with

considerable detail using spectroscopic and microscopic techniques. Double-walled CNTs (DWCNTs) were produced in bulk by Guiderdoni et al., adopting SPS at 1100 °C and 100 MPa pressure [133]. According to reporting requirements, DWCNTs remained intact under those conditions. Extensive molecular dynamic simulations have been used to better study welding of CNTs that resulted in interconnected constructions. The Ozden team previously investigated how density and CNT structure are affected mechanically, electrically, and in terms of hydrophilicity (Figure 13) [134]. Al-Hakami et al. in 2013 investigated an approach to remove *Escherichia coli* (*E. coli*) bacteria from water using both naturally occurring CNTs and modified/functionalized CNTs containing 1-octadecanol groups (C18). As per their findings, *E. coli* was removed by CNT alone by 3–5%; however when paired with microwave radiation, unmodified CNT was able to remove up to 98% of bacteria. When CNT-C18 was employed in similar conditions, the bacteria had been removed by 100% [135]. Most textile wastewater is harmful and non-biodegradable. Semiconductor catalysts can be utilized to treat the environmental contamination. TiO_2 is a significant photocatalyst; unfortunately, TiO_2 has a limited spectrum of light sensitivity and poor efficiency. However, TiO_2 and CNT together can boost photocatalytic activity [136]. Using MWCNT and Ti as source materials, Ming-liang et al. synthesized a CNT- TiO_2 composite in 2009 to accelerate the photocatalytic oxidation of water contaminants [137]. The composite's photoactivity was assessed through the conversion of methylene blue in liquid phase under UV radiation. Researchers came to the conclusion that the CNT- TiO_2 composite's ability to remove methylene blue is facilitating the transfer of electrons between MWCNT and TiO_2 , as well as MWCNT adsorption and TiO_2 photodegradation.

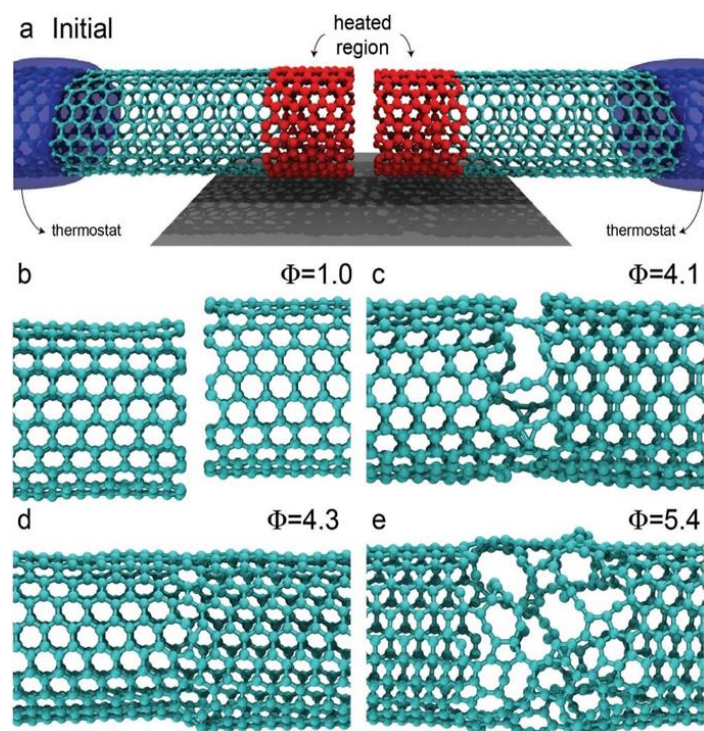


Figure 13. (a) Two CNTs are first arranged with their axes aligned at 180°. The atoms in red are heated from outside and are located at the contact tips of both tubes. (b–e). The tubes' final configuration following heating with heat fluxes of 1.0, 4.1, 4.3, and 5.4 kcal mol⁻¹ fs⁻¹, respectively. Reprinted with permission from Ref. [134]. Copyright © 2016, John Wiley and Sons.

In 2016, Jauris et al. reported a relationship between SWCNTs and two artificial dyes (methylene blue and acridine orange) [138]. Because of π - π interactions' prevalence between each dye and the nanotubes, the researchers reached a conclusion that long-term configuration stability was where the dye is generally plano-parallel to the nanotube. SWCNT

is a prospective adsorbent for dye degradation and could be employed commercially for treating wastewater. By increasing the nanotube's radius, the dye-nanotube binding energy increases. In order to prepare Au-TiO₂@CNT composite photocatalysts for photocatalytic gaseous styrene removal, Zhang W. et al. used a simple micro/nano-bubble approach [139]. High ternary-structure stability can be formed by reacting Au, and TiO₂ NPs coated onto CNTs can be efficiently facilitated by the micro/nano-bubbles. The response surface central composite design approach has been applied to examine Au-TiO₂@CNTs' photoactivity. Rapid development of a compact structure increased the photocatalytic degradation and mineralization of styrene over Au-TiO₂@CNTs dramatically as the reaction temperature increased. The increased photocatalytic mechanism of Au-TiO₂@CNTs was further disclosed through the examination of EPR, UV-vis DRS, electrochemical characteristics, and TPD-O₂. The further identification of free radicals revealed that oxidative radicals like hydroxyls and superoxides were closely related to the photocatalytic degradation and mineralization of styrene, which was primarily because of CNT and Au NP synergistic influence for increased activity through the photocatalysis process.

7. CO₂ Hydrogenation into Hydrocarbons and Oxygenated Hydrocarbons

Under certain conditions, it is thought that CO₂ catalytic hydrogenation with renewable hydrogen is an appropriate method for the chemical recycling of this hazardous and chemical resistance molecule into energy-carrying agents and chemical compounds. With a precise hydrogenation product, CO₂ can be hydrogenated into C₁ compounds like methane and methanol. It is more difficult to produce high (C₂₊) hydrocarbons and oxygenates on a selective basis. Due to its higher volumetric energy density within a specific volume and compatibility with the current fuel infrastructure than C₁ compounds, such produced materials are desirable as entry platform chemicals and energy vectors [140]. The main challenge is integrating catalytic functions as effectively as possible for both the reductive and chain-growth stages [141]. The transformation of renewable energy also makes use of CO₂ as an energy carrier. Because renewable energy sources are intermittent by nature, there is presently a need for scalable storage [142]. Consequently, a much more practical and easier method for storing significant volumes of intermittent energy generated from renewable sources for longer durations is the generation of synthetic natural gas or liquid fuels. The power to gas (PtG) concept has received considerable attention, as seen in Figure 14 [143]. An alternate source of natural gas is produced when CO₂ combines with H₂, which is created by water electrolysis using renewable wind or solar energy. In Copenhagen, especially in 2016, a commercial-scale PtG project with 1.0 MW of capacity had been operating and successfully exploiting the transition to a sustainable energy system [144]. In the period 2003–2009, with capacities ranging from 25–6300 kW, there were five initiatives in Germany utilizing CO₂ methanation at pilot-plant or commercial scale [145]. The French chemist Paul Sabatier published his first study on CO₂ methanation in 1902 [146]. This age-old craft has gained fresh traction as a result of the growing need to combat global climate change and store excess renewable energy. The Sabatier reaction is an excellent method for converting CO₂ into chemical feedstocks and fuels, storing renewable energy sources like wind and solar energy, and efficiently converting biogas to biomethane [147]. CO₂ methanation is an endothermic reaction with higher equilibrium conversion between 25 and 400 °C [148]. By using the right catalysts, CO₂ methanation can achieve 99% CH₄ selectivity, avoid further product separation, and get around the challenges of dispersed product distribution. As a result, such a thermodynamic characteristic increases the importance of CO₂ methanation in terms of energy effectiveness and commercial viability.

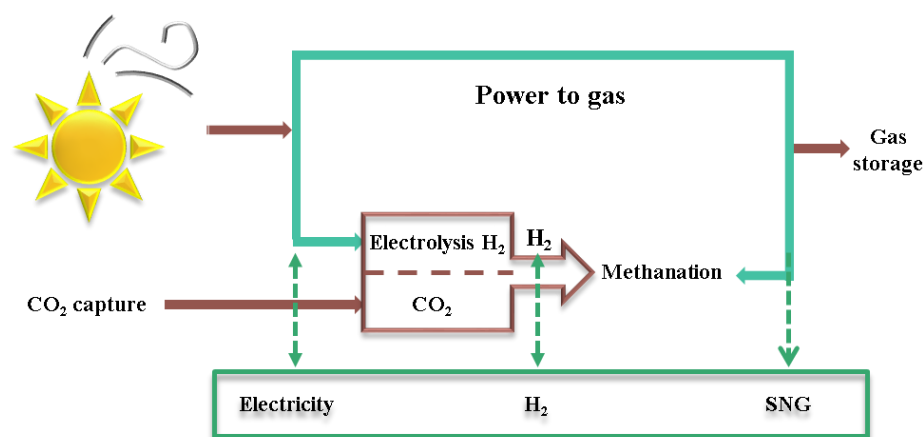


Figure 14. Chemical compounds and fuels produced sustainably using CO₂. At various temperatures, the equilibrium conversion of CO₂ to methane is plotted from the previous literature data.

In order to synthesize C₂₊ hydrocarbons, Fujiwara et al. (2015) investigated CO₂ hydrogenation over composite catalytic compounds made of Cu-Zn-Al oxide catalyst and HB zeolite via combining the production of methanol over Cu-Zn-Al oxide and the simultaneous conversion of methanol over HB zeolite [149]. The yield of C₂₊ hydrocarbons was low (0.5 C-mol%) and lower than that of oxygenated compounds when a non-modified zeolite was employed for the composite catalyst (methanol and dimethyl ether). For the conversion of dimethyl ether to C₂₊ hydrocarbons, the strong acid sites of zeolite were severely inactivated. The catalytic activity of the associated composite catalysts was significantly enhanced by the use of zeolites treated with 1,4-bis(hydroxydimethylsilyl) benzene to create C₂₊ hydrocarbons in yields of more than 7C-mol%. Under a pressure of 0.98 MPa, the best C₂₊ hydrocarbon production selectivity was approximately 12.6 C-mol%. Hydrophobic zeolites with water contact angles more than 130° were created by the disilane modifications. The disilane molecule was converted into a few condensed aromatics during CO₂ hydrogenation at 300 °C, although the hydrophobicity was maintained even after the reaction. The hydrophobic surface of the HB zeolite inhibits the deactivation of the strong acid sites, increasing catalytic activity. Even under low pressure situations, this enhanced composite catalyst will support the synthesis of C₂₊ hydrocarbons from CO₂.

In 2017, Zhang et al. suggested a procedure to create ethanol from paraformaldehyde, CO₂, and H₂ [150]. Under benign conditions, a ruthenium–cobalt (Ru-Co) bimetallic catalyst using LiI as the promoter in 1,3-dimethyl-2-imidazolidinone (DMI) may effectively speed up the process. Overall products had a selectivity of 50.9 C-mol% for ethanol, which was obviously higher than that of the disclosed methods. Additionally, the TOF for ethanol based on Ru metal reached a maximum of 17.9 h^{−1} as seen in Figure 15.

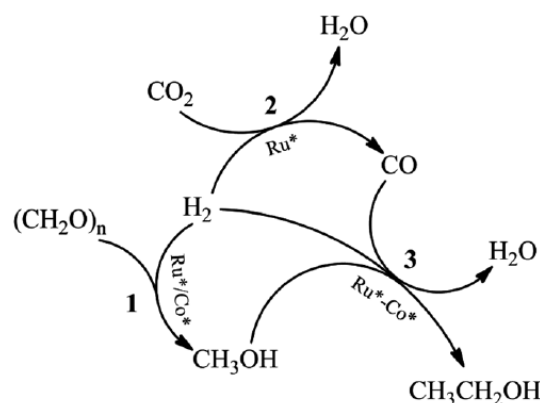


Figure 15. Synergy between the processes used to fabricate ethanol from paraformaldehyde, CO_2 , and H_2 . The active species of Ru and Co are represented, respectively, by Ru^* and Co^* . Reprinted with permission from Ref. [150]. Copyright © 2017, Royal Society of Chemistry.

Significant information about the involvement of oxygen in the electrochemical reduction of CO_2 on Cu electrodes was presented in 2017 by Le Duff and colleagues. They also regulated the surface structure and composition of Cu single crystal electrodes over time [151]. Since the pulse sequence may be controlled to ensure consistent beginning conditions for the reaction at every fraction of time and at a certain frequency, this was accomplished using pulsed voltammetry. Compared to the selective CO_2 reduction achieved using cyclic voltammetry [152], and chronoamperometric techniques [153], under alternating voltage, a wide range of oxygenated hydrocarbons was discovered. The coverage of oxygen species, which is reliant on surface structure and potential, was linked to product selectivity towards the synthesis of oxygenated hydrocarbon. A nanowire-like WSe_2 -graphene catalyst was created by Ali and Oh in 2017 and examined for its ability to photocatalytically convert CO_2 into CH_3OH when exposed to UV-visible light. XRD, SEM, TEM, Raman, and XPS were used to further characterize the produced nanocomposite. Using gas chromatography (GCMS-QP2010SE), the photocurrent analysis was further evaluated for its photocatalytic reduction of CO_2 . The sacrificial agent (Na_2S - Na_2SO_3) was added to WSe_2 -graphene nanocomposite to further increase the photocatalytic effectiveness, and it was discovered that this improved the photocatalytic efficiency, with the methanol output reaching $5.0278 \text{ mol g}^{-1} \text{ h}^{-1}$ [154]. In a different study, Biswas et al. (2018) reported using ultrasonic techniques to create a WSe_2 -Graphene- TiO_2 ternary nanocomposite [155]. According to estimates, the WSe_2 -Graphene- TiO_2 band-gap is 1.62 eV, which is adequate for the photocatalytic degradation when exposed to UV-visible light. For the conversion of CO_2 to CH_3OH , the photocatalytic capability of nanocomposites was examined. After 48 h, WSe_2 -G- TiO_2 with an optimal graphene loading of 8 wt% shown high photoactivity, yielding a total CH_3OH yield of $6.3262 \text{ mol g}^{-1} \text{ h}^{-1}$. The gradual synergistic relationship between the WSe_2 - TiO_2 and graphene components in the heterogeneous system is what causes this exceptional photoreduction activity. Ethylene could be produced from CO_2 electroreduction; however, present systems are constrained by low conversion efficiency, slow production rates, and unstable catalysts. In contrast to a reversible hydrogen electrode (RHE), Dinh et al. (2018) found that a copper electrocatalyst at an abrupt reaction interface in an alkaline electrolyte converts CO_2 to ethylene with a 70% faradaic efficiency (FE) at a potential of -0.55 volts [156]. The activation energy barriers for CO_2 reduction and carbon monoxide (CO)-CO coupling are lowered by hydroxyl ions on or near the copper surface, and as a result, ethylene evolution begins at -0.165 volts versus an RHE in 10 molar potassium hydroxide virtually concurrently with CO generation. By sandwiching the reaction interface between different hydrophobic and conductive supports, a polymer-based gas diffusion layer was introduced to increase operational stability while maintaining continuous ethylene selectivity over the first 150 operating hours. In 2019, Ma and Porosoff proposed reaction mechanisms by combining in situ characterization techniques with DFT

calculations, identifying structure–property relationships for the zeolite support, strategizing methods to increase catalyst lifetime, and developing advanced synthesis techniques for depositing a metal-based active phase within a zeolite for highly active, selective, and stable tandem catalysts [157]. The critical research topics of reaction mechanism elucidation by combining in situ characterization methods with density functional theory calculations, identifying structure–property relationships for the zeolite support, developing advanced synthesis techniques for depositing a metal-based active phase within a zeolite for highly active, selective, and stable tandem catalysts, and strategizing methods to extend catalyst lifetime, are suggested as future research directions. An appealing method for storing such a renewable energy source in the form of chemical energy is the conversion of CO₂ into hydrocarbons using solar energy. A system that couples a photovoltaic (PV) cell to an electrochemical cell (EC) for CO₂ reduction can do this. Such a system should have minimum energy losses related to the catalysts at the anode and cathode, as well as the electrolyzer device, in order to be advantageous and usable. It should also use inexpensive and easily processed solar cells. All of these factors were taken into account by Huan et al. in 2019 when setting up a reference PV-EC system for CO₂ reduction to hydrocarbons [158]. Combined with a fairly priced, state-of-the-art perovskite photovoltaic minimodule, this system sets a standard for a low-cost, all-earth-abundant PV-EC system with a solar-to-hydrocarbon efficiency of 2.3%. In 2019, Wu et al. demonstrated cobalt phthalocyanine (CoPc) catalysis for the six-electron reduction of CO₂ to methanol with considerable activity and selectivity when immobilized on CNTs [159]. They discovered that the conversion produces methanol with FE > 40% and a partial current density exceeding 10 mm/cm² at −0.94 volts with respect to the reversible hydrogen electrode in a near-neutral electrolyte. CO serves as an intermediary in a special domino mechanism that moves the conversion along. By adding amino substituents that donate electrons to the phthalocyanine ring, it is possible to prevent the harmful reduction of the phthalocyanine ligand from having a negative effect on the catalytic activity. With significant activity, selectivity, and stable performance for at least 12 h, the enhanced molecule-based electrocatalyst converts CO₂ to methanol.

A novel multifunctional catalyst made of Fe₂O₃ encapsulated in K₂CO₃ was introduced by Ramirez et al. in 2019 and has the ability to use a tandem process to convert CO₂ into olefins [160]. The authors established that, unlike the conventional systems in FT processes, very large K loadings are essential to activate CO₂ via the well-known “potassium carbonate mechanism.” While utilizing CO₂ as a feedstock, the suggested catalytic process proved to be just as productive as currently used commercial synthesis gas-based techniques. By employing Cu-doped MgAl₂O₄ (Mg_{1−x}Cu_xAl₂O₄) and a straightforward deposition–reduction process, Tada et al. in 2020 investigated the synthesis of Cu NPs. The following three Cu²⁺ species were present in Mg_{1−x}Cu_xAl₂O₄ [161]: short O-Cu octahedrally coordinated [CuO₆]_s, elongated O-Cu octahedrally coordinated [CuO₆]_{el}, and tetrahedrally coordinated [CuO₄]_t. The first two were discovered in Mg_{1−x}Cu_xAl₂O₄ of the inverse-spinel type, and the third was discovered in Mg_{1−x}Cu_xAl₂O₄ of the normal-spinel type. In addition, they made it clear that their percentage is related to Cu loading by concentrating on the variation in the reducibility of the Cu²⁺ species. Mg_{1−x}Cu_xAl₂O₄ predominantly comprised the [CuO₆]_s species at low Cu loading ($x < 0.3$). In contrast, the fraction of the [CuO₆]_{el} and [CuO₄]_t species rose with high Cu loading ($x \geq 0.3$). Notably, the H₂-reduced Mg_{0.8}Cu_{0.2}Al₂O₄ ($x = 0.2$) catalyst showed the best photocatalytic activity among the synthesized catalysts because it had the most exposed metallic Cu sites. Therefore, the formation of metallic Cu NPs on metal oxides depends on the H₂ reduction of [CuO₆]_s.

In 2021, Tada et al., suggested bifunctional tandem ZnZrO_x catalysts for the hydrogenation of CO₂ to methanol along with a number of solid acid catalysts (for subsequent methanol conversion to light olefins) [162]. Researchers used zeolites and silicoaluminophosphates with a variety of topologies, including MOR, FER, MFI, BEA, CHA, and ERI, as solid acid catalysts. A study using ammonia adsorption revealed that they likewise

displayed the equivalent acid characteristics. Lower olefins were being synthesized in one step using the tandem catalysts, whereas with ZnZrO_x alone, no hydrocarbons could be produced. There appears to be no relationship between product yields and acid strength, at least according to the reaction test and ammonia adsorption. The product selectivity is influenced by the pore sizes and the channel dimensionality of the zeolites; zeolites with small pores, like MOR, SAPO-34, and ERI, are promising, whereas zeolites with bigger pores, like MFI, generate heavier hydrocarbons. The outcomes offer fresh perspective on the creation of creative catalysts for CO_2 usage. A low-temperature atmospheric surface dielectric barrier discharge reactor that converts biogas into liquid chemicals was introduced by Rahmani et al. in 2021 [163]. The effect of steam on the conversion of methane and CO_2 was investigated, as well as the distribution of products in relation to a given energy input based on the operational circumstances. The authors reported conversion rates of 44% for CH_4 and 22% for CO_2 . When steam was introduced at the in-feed, the lowest energy cost of 26 eV/molecule was attained. For liquid hydrocarbons, a selectivity of 3% was attained. The transformation of biogas ($\text{CH}_4 + \text{CO}_2$) resulted in the production of more than 12 compounds. At ambient temperature, the most prevalent oxygenated hydrocarbon liquids were acetone, methanol, ethanol, and isopropanol. H_2 , CO , C_2H_4 , and C_2H_6 were the major gases produced.

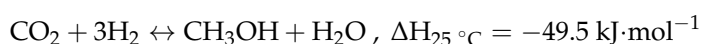
In order to explain an alternative approach for the chemical CO_2 reduction reaction, Islam et al. in 2021 subjected up to 3% CO_2 -saturated pure water, NaCl, and artificial seawater solutions to high-power ultrasound (488 kHz ultrasonic plate transducer) [164]. The converted CO_2 products under ultrasonic settings were discovered to be mostly CH_4 , C_2H_4 , and C_2H_6 , as well as a significant amount of CO that was later converted into CH_4 . The analysis revealed that adding molecular H_2 to the CO_2 conversion process is essential, and that raising the hydrogen concentration boosted hydrocarbon yields. However, it was found that the overall conversion decreased at higher hydrogen concentrations because hydrogen, a diatomic gas, is known to reduce cavitation activity in liquids. Additionally, it was discovered that the maximum hydrocarbon yields (nearly 5%) were achieved with 1.0 M NaCl solutions saturated with 2% $\text{CO}_2 + 98\% \text{H}_2$, and that increasing salt concentrations further decreased the yield of hydrocarbons due to the combined physical and chemical effects of ultrasound. By diluting the flue gas with hydrogen, it was demonstrated that the CO_2 present in a synthetic industrial flue gas (86.74% N_2 , 13.5% CO_2 , 0.2% O_2 , and 600 ppm of CO) could be transformed into hydrocarbons. Additionally, it has been demonstrated that the conversion process can be carried out in ambient circumstances, i.e., at room temperature and pressure, without the use of catalysts, when low-frequency, high-power ultrasound is used. Tian et al. in 2022 newly manufactured In_2O_3 , $\text{MnO-In}_2\text{O}_3$, and $\text{MgO-In}_2\text{O}_3$ catalysts using the co-precipitation method, and they looked into the hydrogenation of CO_2 to methanol [165]. The ability of In_2O_3 to absorb CO_2 was significantly improved by the addition of Mn and Mg oxides. The CO_2 adsorption capacity and the changing trend of methanol selectivity were consistent. As opposed to In_2O_3 , the methanol selectivity of $\text{MnO-In}_2\text{O}_3$ and $\text{MgO-In}_2\text{O}_3$ catalysts is higher. ODP, or oxidative dehydrogenation of propane with CO_2 , is a promising solution for efficient CO_2 usage. In a new study published in 2022, Chernyak et al. included various C-materials for the first time as supports for Cr-based catalysts of CO_2 -assisted ODP [166]. A commercially available activated carbon was evaluated alongside CNTs, jellyfish-like graphene nanoflakes, and their oxidized and N-doped derivatives. The oxidized CNT- and pure GNF-supported catalysts showed the highest activity and a propylene yield of up to 25%. Raman spectroscopy was used to confirm that these two catalysts were stable throughout tests against disintegration and particle sintering. The oxidized CNT- and pristine graphene nanoflakes-supported catalysts' high activity and durability were explained by their macro- and mesoporosity, which improve reagent and product diffusion, as well as by the highest surface graphitization degree, which was validated by XPS. These catalysts performed significantly better than the catalyst supported by activated carbon. As a result, CNTs and graphene nanoflakes are

suitable supports for CO₂-ODP catalytic compounds. Several main catalysts used in the hydrogenation of CO₂ to hydrocarbon were summarized in Table 1.

Table 1. Some of the main catalysts used in the hydrogenation of CO₂ to hydrocarbon products.

Catalysts	Metal/Metal-free	Preparation Method	Process Type	Conversion	Selectivity
Cu-Zn-Al oxide and HB zeolite	Metal	Co-precipitation method	The production of C ₂₊ hydrocarbons by CO ₂ hydrogenation.	2.8%	12.6 C-mol%
Ru-Co	Metal	-	The production of ethanol from paraformaldehyde, CO ₂ , and H ₂	-	50.9 C-mol%
WSe ₂ -graphene	Metal	Ultra-sonication method	Photocatalytic reduction of CO ₂ into CH ₃ OH	5.0278 $\mu\text{mol g}^{-1} \text{h}^{-1}$	-
WSe ₂ -graphene-TiO ₂	Hybrid	Ultra-sonication method	CO ₂ reduction to CH ₃ OH	6.3262 $\mu\text{mol g}^{-1} \text{h}^{-1}$	-
hydroxide-mediated Cu	Metal	Hydroxide-mediated abrupt reaction interface	CO ₂ conversion to ethylene	70%	65%
CoPc/CNT	Hybrid	CO ₂ reduction to methanol	Dispersion process	40%	-
Fe ₂ O ₃ @K ₂ CO ₃	Metal	CO ₂ conversion to olefins	Mortar mixing	40%	60%

Although the technique of hydrogenating carbon dioxide to produce methanol is inexpensive and environmentally benign, nevertheless, because of the increased stability and inertness of CO₂, this reaction is thermodynamically constrained. The reaction below reveals the process of methanol production.



The reaction is thermodynamically advantageous at low temperatures and high pressure, according to the Le Chatelier's principle. The enhanced thermal stability and chemical inertness of CO₂ means that this method of methanol synthesis requires a high temperature to proceed. Indeed, at elevated reaction temperatures (for example, higher than 240 °C), CO₂ activation and subsequent methanol production are facilitated. However, the higher temperature procedure strongly conflicts with the reaction's thermodynamics. Furthermore, when the reaction is conducted at a higher temperature, undesired byproducts including higher alcohols and hydrocarbons are formed. Similar to this, because the CO₂ hydrogenation process produces methanol, which is a molecular reducing reaction, it is thermodynamically more advantageous at high pressure. By employing various catalysts, various reaction pressure sizes have been suggested for the best CO₂ conversion [140].

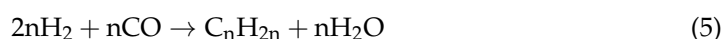
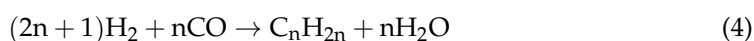
8. Mechanism of Conversion

Alternative catalytic routes for CO₂ fixing into chemicals have the disadvantage of not being connected to the well-established array of technologies for the conversion of syngas mixtures (CO + H₂) into synthetic liquid fuels and platform chemicals. Hydrogenation routes, on the other hand, have the advantage of being connected to these technologies and could, therefore, first achieve an on-purpose CO₂-recycling industrial application. CO₂ hydrogenation is being used to create a variety of different chemicals [141]. CH₄ and CH₃OH, which seem to be important examples of compounds that could be produced by

established or industrial-scale technologies like the methanation and methanol synthesis processes, have received the majority of research attention. Another C_1 product that has already received attention is the derivative dimethyl ether, which would also be formally a C_1 product. Nevertheless, due to a number of factors, high (C_{2+}) hydrocarbons and alcohols, whose production is essentially thermochemically more favorable than that of methanol, may be more desirable products [161]. If somehow the major aim of the hydrogenation process should be applied to produce energy carriers, then lengthening the products' carbon chains will result in ever-higher volumetric energy densities. By directly injecting short-chain alkanes (C_2 – C_4) into gas distribution networks, it is possible to raise the calorific value of natural gas or biogas. Furthermore, average volumetric concentration limits for ethane, propane, and butane in conventional pipeline specifications are around 10, 5, and 2%, respectively [167]. Under ambient conditions, the liquid higher alkanes (C_{5+}) [168], are quite desirable as predecessors of, e.g., jet fuels, because they combine higher energy densities with complete compliance to current liquid-fuel distribution and end-use infrastructures. Base chemical compounds with a chain length between C_2 and C_4 and considered light olefins [169], for the creation of polymers, are an illustration. Regarding oxygenated products, C_{2+} alcohols have higher energy densities than methanol and are less poisonous and corrosive. As a result, they are better suited for use in existing internal combustion engines as blending fractions or even as pure fuels. In addition, strong alcohols like ethanol and butanol are great precursors for short-chain (C_2 – C_4) olefins [170], which, when manufactured very selectively through alcohol dehydration under relatively uncomplicated reaction conditions, can be added to the value chains already in place. Overviews on the catalytic hydrogenation of CO_2 have been published in earlier surveys of the literature [171]. Processes for the manufacturing of C_1 products, particularly methane and methanol and its derivatives, have undergone more concentrated changes [172].

Attention should be paid to the opportunities and intrinsic kinetic constraints, sometimes intimately connected to thermodynamic bounds, that exist for certain catalytic systems and which must be taken into account in the creation of new catalysts and procedures [173].

Due to its capacity to generate clean hydrocarbons like CO, CH_4 , and C_{2+} products, carbon dioxide hydrogenation is a potential reaction that is being studied. Through thermal, photocatalytic, and photothermal catalysis, hydrogenation reactions can move forward. First, CO_2 will be hydrogenated in the Reverse Water Gas Shift (RWGS) reaction (Equation (1)) to yield CO. Then, CH_4 can be created by either directly methanizing CO_2 through the Sabatier reaction (Equation (3)) or further hydrogenating CO (Equation (2)). Both the CO and CO_2 methanation processes are exothermic and take place at temperatures between 200 and 500 °C. Other than that, the Fischer–Tropsch process can be used to create paraffins (alkanes) and olefins (alkenes), which are both significant and pricey chemical feedstocks. Additionally, because they are volume-reducing reactions, a rise in pressure favors the production of CO and hydrocarbon products. This is because, in accordance with Le Chatelier's principle, the equilibrium will change as pressure rises to favor the side of the reaction that contains less moles of gas. Most significantly, as the pressure of the reactor was raised from ambient pressure to 4 bar, the CO_2 methanation activity over RuF catalyst was improved. Additionally, it was noted that the reduction in apparent activation energy caused by the pressure rise helped the methanation reaction progress [174].



Examples of Conversion Mechanisms

Liu et al. examined the advancement of CO₂ direct hydrogenation to value-added compounds such as CO [175], CH₃OH [154], CH₄ [176], DME [177], higher hydrocarbons [178], and olefins [27]. There has also been a summary of heterogeneous catalysis, plasma catalyst supports, and CO₂ hydrogenation research activities [179–181]. A method to increase the oxygen vacancies of nickel-based catalysts for CO₂ methanation was reported by Zhu et al. in 2021 [182–184]. At low reaction temperatures (300 °C), a Y₂O₃-promoted NiO-CeO₂ catalyst was developed and found to have a remarkable methanation activity that is up to three times higher than NiO-CeO₂ and six times higher than NiO-Y₂O₃. The addition of Y₂O₃ to CeO₂ significantly speeds up the production of surface oxygen vacancies during the reaction, as researchers showed both theoretically and experimentally. That study also demonstrated that these regions support CO₂ dissociation directly, which is kinetically more advantageous than associative routes. As a result, it significantly increased the activity of CO₂ methanation. In the feed stream including methane and traces of H₂S, Gac et al. in 2021 discussed CO₂ methanation over ceria- and alumina-supported nickel catalysts in [185]. With a packed-bed reactor, stability tests conducted for 20 h at 350 and 600 °C revealed the catalysts' great resistance to sintering processes. At 350 °C, a higher conversion has been seen for the nickel catalyst assisted by ceria. According to a thermodynamic analysis, under certain reaction conditions, the CO₂ present in biogas can be transformed to methane without carbon production. The decrease in CO₂ conversion and increase in CH₄ selectivity were caused by the addition of CH₄ to the CO₂-H₂ feed stream. When trace amounts of H₂S were added to the feed stream, CO₂ conversion and CH₄ selectivity quickly decreased. Al₂O₃-supported catalysts were shown to be more durable (20%) than CeO₂-based catalysts. Heterogeneous nanocatalytic compounds' atomic usage and activity are typically improved as their size is decreased in a variety of catalytic reactions. This method has, however, been less successful for Cu-based electrocatalysts in the reduction of CO₂ to multi-carbon (C₂₊) products because of the excessively strong intermediate binding to small-sized (15 nm) Cu NPs. Here, Chang et al. in 2022 effectively added pyrenyl-graphdiyne (Pyr-GDY) to ultrafine (2 nm) Cu NPs to give them a greatly increased selectivity for CO₂-to-C₂₊ conversion [186]. By adjusting the catalyst d-band center, Pyr-GDY would be aided in reducing the excessively tight binding between adsorbed H* and CO* intermediates on Cu NPs as well as maintain the ultrafine Cu NPs due to a higher affinity between alkyne moieties and Cu NPs. In comparison to support-free Cu NPs of C₂₊ 20% FE, CNT-supported Cu NPs of 18% C₂₊ FE, GO-supported Cu NPs of 8% C₂₊ FE, and other reported ultrafine Cu NPs, the resultant Pyr-GDY-Cu catalytic composite gave up to 74% FE for C₂₊ products. Their findings highlight the crucial role graphdiyne plays in the selectivity of Cu-catalyzed CO₂ electroreduction and highlight the potential of ultrafine Cu NP catalysts to transform CO₂ into a product with added value (C₂₊). Kattel et al. (2016) used DFT calculations to identify the mechanism of CO₂ hydrogenation at the metal-oxide contacts [187]. In experiments on PtCo-TiO₂ and PtCo-ZrO₂, *HCOO and *HOCO were both shown to be reaction intermediates, but *CH₃O was only found on PtCo-ZrO₂.

9. Theoretical Studies of CO₂ Conversion

DFT calculations were performed by Kumari et al. in 2016 to study the mechanisms of CO₂ reduction to CO and the hydrogenation of CO₂ to methanol on both the stoichiometric and reduced CeO₂(110) surfaces [188]. It was found that CO₂ dissociates to CO through interaction with the oxygen vacancy on the reduced ceria surface, and the produced CO can be further hydrogenated to methanol. In 2016, Cheng et al. investigated the conversion of CO₂ to methanol on the reduced CeO₂(110) surface by performing DFT calculations corrected by on-site Coulomb interaction (DFT + U) and microkinetic analysis [189]. They also found that the HCOO route is the dominant pathway for methanol formation on the reduced CeO₂(110). DFT studies show that the energy required to hydrogenate CO to *CHO on PtCo-TiO₂ is substantially lower than that required to desorb it. The result was a selective generation of CO since the chemisorbed CO preferred energetic desorption over

the subsequent hydrogenation. Mostly on PtCo-ZrO₂ catalysts, however, CO generation was hampered, and CH₄ was produced instead. Chai and Guo demonstrated in 2016 that the interaction of N-doping and curvature can successfully control the activity and selectivity of graphene-CNT catalysts using both DFT and ab initio molecular dynamic calculations [190]. For graphitic N-doped graphene edges, as opposed to the un-doped equivalent, the CO₂ activation barrier can be adjusted to 0.58 eV. While the (6, 0) CNT with a high degree of curvature is efficient for both CH₃OH and HCHO synthesis, the graphene catalyst without curvature demonstrated great selectivity for CO-HCOOH generation. Curvature played a significant role in adjusting the overpotential for a particular product, e.g., for the synthesis of CO, from 1.5 to 0.02 V, and for CH₃OH, from 1.29 to 0.49 V. Thus, as demonstrated here for CO₂ reduction, graphene-CNT nanostructures provide significant scope and flexibility for effective tuning of catalytic efficiency and selectivity. Green chemistry is a fascinating field that deals with chemicals like ethanol produced from CO₂ transformation. Li et al. in 2019 investigated the mechanism of thermal catalytic hydrogenation of CO₂ to methanol on reduced CeO₂(100) by using DFT calculations [191]. They found that CO₂ was hydrogenated via the HCOO route rather than the COOH route. These results then indicate that oxygen vacancies on the reduced CeO₂ surface are crucial to the conversion of CO₂ to CH₃OH.

The combined experimental and density functional theory (DFT) study of Liu et al. in 2020 reported that the morphology control of CeO₂ nano-catalysts is important for methanol synthesis [192]. They also proposed that methanol was likely generated via the so-called formate (HCOO) pathway where the adsorbed CO₂ is firstly hydrogenated to the HCOO* species. In 2020, Coufourier et al. created a catalytic system that was both effective and affordable [193]. The CO₂ reductions, hydrogenocarbonate, and carbonate in pure water were described for use in an iron catalyst system that is very effective, has higher stability, is free of phosphine, and is simple to produce. Carbonic derivative hydrogenation occurs in good yields with good catalytic performance in just the existence of the bifunctional cyclopentadienone iron tricarbonyl. For the hydrogenation of CO₂, hydrogenocarbonate, and carbonate into formate in pure water, turnover numbers (TON) of up to 3343, 4234, and 40, respectively, have been obtained. Cao et al. in 2021 coupled the DFT calculations with micro-kinetic modeling [194]. The lack of interactions between adsorbed formate and intermediates, which would understate the rate of CO₂ pathway by possessing a too high formate coverage, was shown to be the cause of the discrepancy between the investigational rate and the earlier simulated predictions in the literature. The researchers demonstrated that CO₂ hydrogenation dominates for pure Cu catalysts, which is consistent with results, when adsorbate–adsorbate interactions, particularly the generated H bond, were considered. In particular, it has been found that the adsorbed HCOOH* can hydrogenate in a new transition state that is already being stable by hydrogen bonds. In an earlier study in 2022, Rasteiro et al. applied DFT calculations to analyze the impact of alloy–support synergy on the catalytic performance of Ni₅Ga₃ supported by SiO₂, CeO₂, and ZrO₂ [195]. The most promising catalyst, Ni₅Ga₃-ZrO₂, had a reaction mechanism that the researchers proposed according to DFT results. In 2022, Kovalskii et al. examined Au-h-BN(O) and Pt-h-BN(O) nanohybrids in CO oxidation and CO₂ hydrogenation reactions, and on the basis of DFT calculations, postulated potential catalytic reaction pathways [196]. Oxygen-related chemical reactions were accelerated by a charge density distribution at the Pt-h-BN interface via increasing oxygen absorption. In order to elucidate the mechanism underlying the catalysis of selective hydrogenation of CO₂ to methanol, Wang et al. in 2022 performed extensive DFT calculations corrected by on-site Coulomb interaction (DFT + U) to investigate the H₂ dissociation and the reaction between the active H species and CO₂ on the pristine and Cu-doped CeO₂(111) (denoted as Cu/CeO₂(111)) surfaces [197]. Their calculations evidenced that the heterolytic H₂ dissociation for hydride generation can more readily occur on the Cu/CeO₂(111) surface than on the pristine CeO₂(111) surface. They also found that the Cu dopant can facilitate the formation of surface oxygen vacancies, further promoting the generation of hydride species. Moreover, the adsorption of CO₂

and the hydrogenation of CO₂ to HCOO* can be greatly promoted on the Cu/CeO₂(111) surface with hydride species, which can lead to high activity and selectivity toward CO₂ hydrogenation into methanol.

10. Preparation and Approximate Cost of CNTs

Table 2 describes the numerous purification steps and the mass variations during each purification stage. Based on this, each step in the purification table is clearly intended to remove some contaminants in order to produce pure CNTs [198]. The definition of “yield” varies considerably from author to author; some claim that yield is based on removing only metallic particles, while others claim that it is based on removing everything extraneous other than the CNTs. The second reason is thought to constitute the foundation for the yield in the current experiment. As a result, although having what seem to be lower yields, the current technique of synthesis has a more cost-effective yield because it is less expensive [199].

Table 2. Purification stages and each stage’s effective mass variation.

Method	Set up	Purity	Cost in USD
Conventional arc discharge in vacuum	TIG power source, inert atmosphere, metal cabinet with water cooling system, automated process, and chemical purification	80–95 wt%	15 USD/gm
Chemical vapor deposition (CVD)	Furnace, inert atmosphere, metal catalyst	95%	40 USD/gm
Laser ablation	Laser source, furnace, inert atmosphere, metal catalyst–graphite composite	20–80 wt%	Due to the high capital cost of the laser and the lower quantity of CNT after final purification, this method is not commercially viable.
Floating catalyst method	Tubular reactor, quartz tube, thermocouples, inert gas	70–90 wt%	It requires a complicated set up. The cost of aromatic hydrocarbons is very high (Benzene: 44 USD/10 g).
Cyclic oxidation	Plant materials, ceramic reactor	No reports on purity	Even though the source materials are cheap, pre-treatment and heating takes longer duration in a high pressure vacuum chamber. Yield details are not available.
EDM process	Plasma sputtering unit, microelectric discharge apparatus, metal catalyst	No reports on purity	It requires costly equipment such as plasma-sputtering unit and microelectric discharge unit. Yield details are not mentioned.
Combustion process	Bunsen burner, liquefied butane, metal catalyst	No reports on purity	This method is simple but the yield seems to be much less compared to other methods (in mg).
Simplified arc discharge in air	Manual metal arc welding machine and chemical purification	75–80 wt%	3 USD/gm

11. CNTs as Catalysts

For catalytic reactions, carbon nanostructures offer a catalytic support framework that demonstrates good adhesion, metal particle stability at high temperatures, and relative chemical inertness [129]. In the past, FT catalysis has been carried out using carbon-based catalysts, including carbon nanotubes. C_{2+} hydrocarbons can now be formed with good selectivity using carbon-based catalysts [149]. Due to the well-stressed and superior graphical nature of the curved support, metal particles placed on carbon nanotubes behave differently from those deposited on flat non-carbon nanosupports. It has been demonstrated that hydrogen spillage from conductive nanoparticles on stents is superior to that from non-conductive analogues. Where there is a physical route for hydrogen to get from the NP to the support surface, bridging happens [189]. As the hydrogen travels to the surface supporting the nanotube, it interacts with the nanoparticles and needs to be stabilized. In the absence of a physical bridge, hydrogen species created by the nanoparticles cannot be transferred to the support surface. The intrinsic capacity of the substrates to support hydrogen species is ruled out in the event of poor transport from the nanoparticles to the surface. Less hydrogen on the nanotube's surface results from decreased hydrogen leakage, which hinders the catalyst's capacity to reduce carbon dioxide or carbon dioxide throughout the reaction [200].

With many more potential uses in the future, CNTs have already found commercial success in the domains of energy storage (such as consumer lithium-ion batteries), coatings and films (such as fouling-resistant paints for ship hulls), and composite materials (such as enhanced wind turbine blades). They are also desired as support materials for catalytic transition metal nanoparticles in the field of chemical catalysis. The high surface area, tunable structure (e.g., diameter, porosity, and surface composition), and excellent chemical and thermal stability of CNTs have all been recognized to make them particularly desirable as catalyst supports. Their surface area, which ranges from 400 to 900 and 200 to 400 $m^2 g^{-1}$ for SWCNTs and MWCNTs, respectively, is desirable because it enables the deposition and dispersion of catalytic metal nanoparticles with a high surface area-to-volume ratio. An sp^2 hybridized network of carbon atoms that forms a tube with a nanometer-scale diameter and often a high aspect ratio is known as a CNT. Due to their many attractive characteristics, CNTs have attracted considerable research attention for uses in everything from construction to electronics, catalysis, and beyond [201].

12. Conclusions

CO_2 is a significant greenhouse gas that, due to its growing atmospheric concentrations, is thought to be the primary cause of both global warming and climate change. As a result, global attention has shifted to CO_2 concentration reduction. The chemical transformation of CO_2 produces carbon compounds that can be used as precursors for the production of chemicals and fuels. The conversion of CO_2 into fuels and chemicals presents options for reducing the rising CO_2 buildup because CO_2 is both a renewable and ecofriendly source of carbon and it can be used as a C_1 building block for valuable chemicals. Studies have shown that increased concentrations of carbon dioxide increase photosynthesis, spurring plant growth. While rising carbon dioxide concentrations in the air can be beneficial for plants, they are also the chief culprit in climate change. There are only three sources of renewable carbon: renewable carbon from the recycling of already existing plastics (mechanical and chemical recycling), renewable carbon obtained from all types of biomass, and renewable carbon from direct CO_2 utilization of fossil point sources (while they still exist), as well as from permanently biogenous point sources and direct air capture. All three sources are essential for a complete transition to renewable carbon, and all of them, in equal shares, should be used by industry, supported by politicians, and accepted by the population. In a sustainable chemical industry, bulk chemicals will primarily rely on chemical CO_2 utilization through methane, methanol, and naphtha, while specialty chemicals and complex molecules will more likely be produced from biomass (and CO_2 fermentation). At the same time, mechanical and chemical recycling will reduce the overall

need for additional renewable carbon. Whereas traditional recycling re-uses products and materials, the use of biomass and direct CO₂ utilization is tantamount to a recycling process, which also constitutes part of an extended circular economy. The hydrogenation of CO₂ is a practical and efficient procedure in this respect, as has already been mentioned in the review. One of the main issues in developing an exergonic CO₂ conversion reaction is thermodynamically unfavorable CO₂ thermochemical properties. This gas is in the highest oxidation state of carbon, which results in its relatively low standard enthalpy of formation. That is the reason for this molecule being one of the main products of combustion reactions. Different technical directions and targeted research methods on the logical design of catalysts, reactor optimization, and investigation of reaction mechanisms have been proposed to overcome the limits on conversion and selectivity. In fact, oxides have been found to be able to overcome the limits on CO₂ conversion into oxygenated hydrocarbons by means of the supported metallic catalysts at moderate temperatures and pressures. Furthermore, the preparation of bifunctional catalysts combining metal oxides and zeolites has demonstrated an effective way to control the product selectivity for the conversion. Graphene and CNT have been extensively studied by academics over the past 15 years as 3D nanostructured materials for catalytic applications because of their impressive chemical and physical properties. There have been numerous reviews of the heterogeneous catalytic hydrogenation of CO₂ that can be categorized by the methods used, such as thermal, electrochemical, and photochemical hydrogenation, as well as by the homogeneous and heterogeneous catalysts used, or by the resulting product distributions or catalysts used. Despite the difficulties, the transformation of CO₂ to value-added chemicals still receives great attention worldwide because of its significance for providing sustainable alternatives to solve urgent issues such as those of energy and the environment. Recent years have seen the emergence of experimental and computational technologies for more efficient search and design of catalysts and other materials. Experimental technologies are increasingly being employed for the rapid discovery of novel catalysts and materials. On the other hand, a similar array of computational technologies, including high-throughput and automated computational simulations and reaction modeling, coupled with machine learning algorithms, have also started to enable the theoretical understanding and prediction of new catalysts.

Author Contributions: Conceptualization, W.N.R.W.I. and L.M.S.; validation, W.N.R.W.I.; formal analysis, L.M.S.; investigation, A.A.-A. and L.M.S.; resources, W.N.R.W.I.; data curation, L.M.S.; writing—original draft preparation, L.M.S.; writing—review and editing, A.A.-A.; supervision, W.N.R.W.I. and A.A.-A.; project administration, W.N.R.W.I. and A.A.-A.; funding acquisition, W.N.R.W.I. All authors have read and agreed to the published version of the manuscript.

Funding: This research was funded by Ministry of Higher Education Malaysia FRGS/1/2020/TK0/UKM/02/31.

Acknowledgments: The authors thank Universiti Kebangsaan Malaysia (Malaysia) and the University of Technology (Iraq) for supporting this work.

Conflicts of Interest: The authors declare no conflict of interest.

References

1. Ma, R.; Xu, B.; Zhang, X. Catalytic partial oxidation (CPOX) of natural gas and renewable hydrocarbons/oxygenated hydrocarbons—A review. *Catal. Today* **2019**, *338*, 18–30. [CrossRef]
2. Hasan, S.Z.; Ahmad, K.N.; Isahak, W.N.R.W.; Pudukudy, M.; Masdar, M.S.; Jahim, J.M. Synthesis, Characterisation and Catalytic Activity of NiO supported Al₂O₃ for CO₂ Hydrogenation to Carboxylic Acids: Influence of Catalyst Structure. *IOP Conf. Ser. Earth Environ. Sci.* **2019**, *268*, 012079. [CrossRef]
3. Palmeri, N.; Chiodo, V.; Freni, S.; Frusteri, F.; Bart, J.; Cavallaro, S. Hydrogen from oxygenated solvents by steam reforming on Ni/Al₂O₃ catalyst. *Int. J. Hydrogen Energy* **2008**, *33*, 6627–6634. [CrossRef]
4. Kahn, B. Earth's CO₂ Passes the 400 PPM Threshold—Maybe Permanently. *Sci. Am.* **2016**. Available online: <https://www.scientificamerican.com/article/earth-s-co2-passes-the-400-ppm-threshold-maybe-permanently/> (accessed on 1 November 2022).
5. Capros, P.; Tasios, N.; De Vita, A.; Mantzos, L.; Paroussos, L. Model-based analysis of decarbonising the EU economy in the time horizon to 2050. *Energy Strat. Rev.* **2012**, *1*, 76–84. [CrossRef]
6. European Commission. *A Roadmap for Moving to a Competitive Low Carbon Economy in 2050*. COM(2011) 112 Final; European Commission: Brussels, Belgium, 2011; Volume 34, pp. 1–34.

7. Dimitriou, I.; García-Gutiérrez, P.; Elder, R.H.; Cuéllar-Franca, R.M.; Azapagic, A.; Allen, R.W.K. Carbon dioxide utilisation for production of transport fuels: Process and economic analysis. *Energy Environ. Sci.* **2015**, *8*, 1775–1789. [\[CrossRef\]](#)
8. Ma, X.; Wang, X.; Song, C. “Molecular Basket” Sorbents for Separation of CO₂ and H₂S from Various Gas Streams. *J. Am. Chem. Soc.* **2009**, *131*, 5777–5783. [\[CrossRef\]](#)
9. Du, G.; Lim, S.; Yang, Y.; Wang, C.; Pfefferle, L.; Haller, G.L. Methanation of carbon dioxide on Ni-incorporated MCM-41 catalysts: The influence of catalyst pretreatment and study of steady-state reaction. *J. Catal.* **2007**, *249*, 370–379. [\[CrossRef\]](#)
10. Duyar, M.S.; Treviño, M.A.A.; Farrauto, R.J. Dual function materials for CO₂ capture and conversion using renewable H₂. *Appl. Catal. B Environ.* **2015**, *168–169*, 370–376. [\[CrossRef\]](#)
11. Lee, C.-Y.; Zhao, Y.; Wang, C.; Mitchell, D.R.G.; Wallace, G.G. Rapid formation of self-organised Ag nanosheets with high efficiency and selectivity in CO₂ electroreduction to CO. *Sustain. Energy Fuels* **2017**, *1*, 1023–1027. [\[CrossRef\]](#)
12. Li, K.; Peng, B.; Peng, T. Recent Advances in Heterogeneous Photocatalytic CO₂ Conversion to Solar Fuels. *ACS Catal.* **2016**, *6*, 7485–7527. [\[CrossRef\]](#)
13. Welch, A.J.; DuChene, J.S.; Tagliabue, G.; Davoyan, A.R.; Cheng, W.-H.; Atwater, H.A. Nanoporous Gold as a Highly Selective and Active Carbon Dioxide Reduction Catalyst. *ACS Appl. Energy Mater.* **2019**, *2*, 164–170. [\[CrossRef\]](#)
14. Xie, H.; Wang, T.; Liang, J.; Li, Q.; Sun, S. Cu-based nanocatalysts for electrochemical reduction of CO₂. *Nano Today* **2018**, *21*, 41–54. [\[CrossRef\]](#)
15. Huang, H.; Jia, H.; Liu, Z.; Gao, P.; Zhao, J.; Luo, Z.; Yang, J.; Zeng, J. Understanding of Strain Effects in the Electrochemical Reduction of CO₂: Using Pd Nanostructures as an Ideal Platform. *Angew. Chem. Int. Ed.* **2017**, *56*, 3594–3598. [\[CrossRef\]](#)
16. Ma, M.; Trzeźniewski, B.J.; Xie, J.; Smith, W.A. Selective and Efficient Reduction of Carbon Dioxide to Carbon Monoxide on Oxide-Derived Nanostructured Silver Electrocatalysts. *Angew. Chem. Int. Ed.* **2016**, *55*, 9748–9752. [\[CrossRef\]](#)
17. Su, P.; Xu, W.; Qiu, Y.; Zhang, T.; Li, X.; Zhang, H. Ultrathin Bismuth Nanosheets as a Highly Efficient CO₂ Reduction Electrocatalyst. *ChemSuschem* **2018**, *11*, 848–853. [\[CrossRef\]](#)
18. Li, Q.; Fu, J.; Zhu, W.; Chen, Z.; Shen, B.; Wu, L.; Xi, Z.; Wang, T.; Lu, G.; Zhu, J.-J.; et al. Tuning Sn-Catalysis for Electrochemical Reduction of CO₂ to CO via the Core/Shell Cu/SnO₂ Structure. *J. Am. Chem. Soc.* **2017**, *139*, 4290–4293. [\[CrossRef\]](#)
19. Hu, X.-M.; Rønne, M.H.; Pedersen, S.U.; Skrydstrup, T.; Daasbjerg, K. Enhanced Catalytic Activity of Cobalt Porphyrin in CO₂ Electroreduction upon Immobilization on Carbon Materials. *Angew. Chem. Int. Ed.* **2017**, *56*, 6468–6472. [\[CrossRef\]](#)
20. Chen, Q.; Tsiakaras, P.; Shen, P. Electrochemical Reduction of Carbon Dioxide: Recent Advances on Au-Based Nanocatalysts. *Catalysts* **2022**, *12*, 1348. [\[CrossRef\]](#)
21. Brouzgou, A.; Song, S.; Liang, Z.-X.; Tsiakaras, P. Non-Precious Electrocatalysts for Oxygen Reduction Reaction in Alkaline Media: Latest Achievements on Novel Carbon Materials. *Catalysts* **2016**, *6*, 159. [\[CrossRef\]](#)
22. Alaba, P.A.; Abbas, A.; Daud, W.M.W. Insight into catalytic reduction of CO₂: Catalysis and reactor design. *J. Clean. Prod.* **2017**, *140*, 1298–1312. [\[CrossRef\]](#)
23. Centi, G.; Perathoner, S. CO₂-based energy vectors for the storage of solar energy. *Greenh. Gases Sci. Technol.* **2011**, *1*, 21–35. [\[CrossRef\]](#)
24. Porosoff, M.D.; Yan, B.; Chen, J.G. Catalytic reduction of CO₂ by H₂ for synthesis of CO, methanol and hydrocarbons: Challenges and opportunities. *Energy Environ. Sci.* **2016**, *9*, 62–73. [\[CrossRef\]](#)
25. Gao, P.; Li, S.; Bu, X.; Dang, S.; Liu, Z.; Wang, H.; Zhong, L.; Qiu, M.; Yang, C.; Cai, J.; et al. Direct conversion of CO₂ into liquid fuels with high selectivity over a bifunctional catalyst. *Nat. Chem.* **2017**, *9*, 1019–1024. [\[CrossRef\]](#) [\[PubMed\]](#)
26. Song, H.; Zhang, N.; Zhong, C.; Liu, Z.; Xiao, M.; Gai, H. Hydrogenation of CO₂ into formic acid using a palladium catalyst on chitin. *New J. Chem.* **2017**, *41*, 9170–9177. [\[CrossRef\]](#)
27. Visconti, C.G.; Martinelli, M.; Falbo, L.; Infantes-Molina, A.; Liotti, L.; Forzatti, P.; Iaquaniello, G.; Palo, E.; Picutti, B.; Brignoli, F. CO₂ hydrogenation to lower olefins on a high surface area K-promoted bulk Fe-catalyst. *Appl. Catal. B Environ.* **2017**, *200*, 530–542. [\[CrossRef\]](#)
28. Larmier, K.; Liao, W.-C.; Tada, S.; Lam, E.; Verel, R.; Bansode, A.; Urakawa, A.; Comas-Vives, A.; Copéret, C. CO₂-to-Methanol Hydrogenation on Zirconia-Supported Copper Nanoparticles: Reaction Intermediates and the Role of the Metal-Support Interface. *Angew. Chem. Int. Ed.* **2017**, *56*, 2318–2323. [\[CrossRef\]](#)
29. Bai, S.; Shao, Q.; Wang, P.; Dai, Q.; Wang, X.; Huang, X. Highly Active and Selective Hydrogenation of CO₂ to Ethanol by Ordered Pd–Cu Nanoparticles. *J. Am. Chem. Soc.* **2017**, *139*, 6827–6830. [\[CrossRef\]](#)
30. Sorcar, S.; Hwang, Y.; Lee, J.; Kim, H.; Grimes, K.M.; Grimes, C.A.; Jung, J.-W.; Cho, C.-H.; Majima, T.; Hoffmann, M.R.; et al. CO₂, water, and sunlight to hydrocarbon fuels: A sustained sunlight to fuel (Joule-to-Joule) photoconversion efficiency of 1%. *Energy Environ. Sci.* **2019**, *12*, 2685–2696. [\[CrossRef\]](#)
31. Tan, Z.; Ni, K.; Chen, G.; Zeng, W.; Tao, Z.; Ikram, M.; Zhang, Q.; Wang, H.; Sun, L.; Zhu, X.; et al. Incorporating Pyrrolic and Pyridinic Nitrogen into a Porous Carbon made from C₆₀ Molecules to Obtain Superior Energy Storage. *Adv. Mater.* **2017**, *29*, 160341. [\[CrossRef\]](#)
32. Chen, J.; Xue, C.; Ramasubramaniam, R.; Liu, H. A new method for the preparation of stable carbon nanotube organogels. *Carbon* **2006**, *44*, 2142–2146. [\[CrossRef\]](#)
33. Navrotskaya, A.G.; Aleksandrova, D.D.; Krivoschapkin, E.F.; Sillanpää, M.; Krivoschapkin, P.V. Hybrid Materials Based on Carbon Nanotubes and Nanofibers for Environmental Applications. *Front. Chem.* **2020**, *8*, 546. [\[CrossRef\]](#)

34. Worsley, M.A.; Shin, S.J.; Merrill, M.D.; Lenhardt, J.; Nelson, A.J.; Woo, L.Y.; Gash, A.E.; Baumann, T.F.; Orme, C.A. Ultralow Density, Monolithic WS₂, MoS₂, and MoS₂/Graphene Aerogels. *ACS Nano* **2015**, *9*, 4698–4705. [\[CrossRef\]](#)
35. Mamba, G.; Mishra, A.K. Graphitic carbon nitride (g-C₃N₄) nanocomposites: A new and exciting generation of visible light driven photocatalysts for environmental pollution remediation. *Appl. Catal. B Environ.* **2016**, *198*, 347–377. [\[CrossRef\]](#)
36. Kovtyukhova, N.I.; Mallouk, T.E.; Pan, A.L.; Dickey, E.C. Individual Single-Walled Nanotubes and Hydrogels Made by Oxidative Exfoliation of Carbon Nanotube Ropes. *J. Am. Chem. Soc.* **2003**, *125*, 9761–9769. [\[CrossRef\]](#)
37. Sun, Y.; Wu, Q.; Xu, Y.; Bai, H.; Li, C.; Shi, G. Highly conductive and flexible mesoporous graphitic films prepared by graphitizing the composites of graphene oxide and nanodiamond. *J. Mater. Chem.* **2011**, *21*, 7154–7160. [\[CrossRef\]](#)
38. Bryning, M.B.; Milkie, D.E.; Islam, M.F.; Hough, L.A.; Kikkawa, J.M.; Yodh, A.G. Carbon Nanotube Aerogels. *Adv. Mater.* **2007**, *19*, 661–664. [\[CrossRef\]](#)
39. Gui, X.; Wei, J.; Wang, K.; Cao, A.; Zhu, H.; Jia, Y.; Shu, Q.; Wu, D. Carbon Nanotube Sponges. *Adv. Mater.* **2010**, *22*, 617–621. [\[CrossRef\]](#)
40. Zhang, L.L.; Xiong, Z.; Zhao, X.S. Pillaring Chemically Exfoliated Graphene Oxide with Carbon Nanotubes for Photocatalytic Degradation of Dyes under Visible Light Irradiation. *ACS Nano* **2010**, *4*, 7030–7036. [\[CrossRef\]](#)
41. Zhu, Y.; Li, L.; Zhang, C.; Casillas, G.; Sun, Z.; Yan, Z.; Ruan, G.; Peng, Z.; Raji, A.-R.; Kittrell, C.; et al. A seamless three-dimensional carbon nanotube graphene hybrid material. *Nat. Commun.* **2012**, *3*, 1225. [\[CrossRef\]](#)
42. Tripathi, M.; Valentini, L.; Rong, Y.; Bon, S.B.; Pantano, M.F.; Speranza, G.; Guarino, R.; Novel, D.; Iacob, E.; Liu, W.; et al. Free-Standing Graphene Oxide and Carbon Nanotube Hybrid Papers with Enhanced Electrical and Mechanical Performance and Their Synergy in Polymer Laminates. *Int. J. Mol. Sci.* **2020**, *21*, 8585. [\[CrossRef\]](#) [\[PubMed\]](#)
43. Liu, J.; Zhang, L.; Bin Wu, H.; Lin, J.; Shen, Z.; Lou, X.W. High-performance flexible asymmetric supercapacitors based on a new graphene foam/carbon nanotube hybrid film. *Energy Environ. Sci.* **2014**, *7*, 3709–3719. [\[CrossRef\]](#)
44. Jin, S.; Xin, S.; Wang, L.; Du, Z.; Cao, L.; Chen, J.; Kong, X.; Gong, M.; Lu, J.; Zhu, Y.; et al. Covalently Connected Carbon Nanostructures for Current Collectors in Both the Cathode and Anode of Li-S Batteries. *Adv. Mater.* **2016**, *28*, 9094–9102. [\[CrossRef\]](#)
45. Peng, Q.; Li, Y.; He, X.; Gui, X.; Shang, Y.; Wang, C.; Wang, C.; Zhao, W.; Du, S.; Shi, E.; et al. Graphene Nanoribbon Aerogels Unzipped from Carbon Nanotube Sponges. *Adv. Mater.* **2014**, *26*, 3241–3247. [\[CrossRef\]](#)
46. Chen, L.; Du, R.; Zhu, J.; Mao, Y.; Xue, C.; Zhang, N.; Hou, Y.; Zhang, J.; Yi, T. Three-Dimensional Nitrogen-Doped Graphene Nanoribbons Aerogel as a Highly Efficient Catalyst for the Oxygen Reduction Reaction. *Small* **2015**, *11*, 1423–1429. [\[CrossRef\]](#) [\[PubMed\]](#)
47. Chen, L.-F.; Zhang, X.-D.; Liang, H.-W.; Kong, M.; Guan, Q.-F.; Chen, P.; Wu, Z.-Y.; Yu, S.-H. Synthesis of Nitrogen-Doped Porous Carbon Nanofibers as an Efficient Electrode Material for Supercapacitors. *ACS Nano* **2012**, *6*, 7092–7102. [\[CrossRef\]](#) [\[PubMed\]](#)
48. Chen, L.-F.; Huang, Z.-H.; Liang, H.-W.; Gao, H.-L.; Yu, S.-H. Three-Dimensional Heteroatom-Doped Carbon Nanofiber Networks Derived from Bacterial Cellulose for Supercapacitors. *Adv. Funct. Mater.* **2014**, *24*, 5104–5111. [\[CrossRef\]](#)
49. Yan, X.; You, H.; Liu, W.; Wang, X.; Wu, D. Free-Standing and Heteroatoms-Doped Carbon Nanofiber Networks as a Binder-Free Flexible Electrode for High-Performance Supercapacitors. *Nanomaterials* **2019**, *9*, 1189. [\[CrossRef\]](#)
50. He, Z.; Yang, Y.; Liu, J.-W.; Yu, S.-H. Emerging tellurium nanostructures: Controllable synthesis and their applications. *Chem. Soc. Rev.* **2017**, *46*, 2732–2753. [\[CrossRef\]](#)
51. Luo, W.; Chen, X.; Wei, Z.; Liu, D.; Yao, W.; Zhu, Y. Three-dimensional network structure assembled by g-C₃N₄ nanorods for improving visible-light photocatalytic performance. *Appl. Catal. B Environ.* **2019**, *255*, 117761. [\[CrossRef\]](#)
52. Ou, H.; Yang, P.; Lin, L.; Anpo, M.; Wang, X. Carbon Nitride Aerogels for the Photoredox Conversion of Water. *Angew. Chem. Int. Ed.* **2017**, *56*, 10905–10910. [\[CrossRef\]](#) [\[PubMed\]](#)
53. Abu-Zied, B.M.; Alamry, K.A. Green synthesis of 3D hierarchical nanostructured Co₃O₄/carbon catalysts for the application in sodium borohydride hydrolysis. *J. Alloy. Compd.* **2019**, *798*, 820–831. [\[CrossRef\]](#)
54. Liu, J.J.; Xu, Y.X. Three-dimensional Graphene-based Composites and Two-dimensional Polymers: Synthesis and Application in Energy Storage and Conversion. *Acta Polym. Sin.* **2019**, *50*, 219–232.
55. Alali, K.T.; Yu, J.; Moharram, D.; Liu, Q.; Chen, R.; Zhu, J.; Li, R.; Liu, P.; Liu, J.; Wang, J. In situ construction of 3-dimensional hierarchical carbon nanostructure; investigation of the synthesis parameters and hydrogen evolution reaction performance. *Carbon* **2021**, *178*, 48–57. [\[CrossRef\]](#)
56. Ferrari, A.C.; Bonaccorso, F.; Fal'Ko, V.; Novoselov, K.S.; Roche, S.; Bøggild, P.; Borini, S.; Koppens, F.H.L.; Palermo, V.; Pugno, N.; et al. Science and technology roadmap for graphene, related two-dimensional crystals, and hybrid systems. *Nanoscale* **2015**, *7*, 4598–4810. [\[CrossRef\]](#)
57. Arjmandi-Tash, H.; Lebedev, N.; van Deursen, P.M.; Aarts, J.; Schneider, G.F. Hybrid cold and hot-wall reaction chamber for the rapid synthesis of uniform graphene. *Carbon* **2017**, *118*, 438–442. [\[CrossRef\]](#)
58. Alnuaimi, A.; Almansouri, I.; Saadat, I.; Nayfeh, A. Toward fast growth of large area high quality graphene using a cold-wall CVD reactor. *RSC Adv.* **2017**, *7*, 51951–51957. [\[CrossRef\]](#)
59. Al-Hagri, A.; Li, R.; Rajput, N.S.; Lu, C.; Cong, S.; Sloyan, K.; Almahri, M.A.; Tamalampudi, S.R.; Chiesa, M.; Al Ghaferi, A. Direct growth of single-layer terminated vertical graphene array on germanium by plasma enhanced chemical vapor deposition. *Carbon* **2019**, *155*, 320–325. [\[CrossRef\]](#)

60. Chen, Y.-C.; Lin, W.-H.; Tseng, W.-S.; Chen, C.-C.; Rossman, G.; Chen, C.-D.; Wu, Y.-S.; Yeh, N.-C. Direct growth of mm-size twisted bilayer graphene by plasma-enhanced chemical vapor deposition. *Carbon* **2020**, *156*, 212–224. [\[CrossRef\]](#)
61. Sohn, K.; Na, Y.J.; Chang, H.; Roh, K.-M.; Jang, H.D.; Huang, J. Oil absorbing graphene capsules by capillary molding. *Chem. Commun.* **2012**, *48*, 5968–5970. [\[CrossRef\]](#)
62. Yan, J.; Ding, Y.; Hu, C.; Cheng, H.; Chen, N.; Feng, Z.; Zhang, Z.; Qu, L. Preparation of multifunctional microchannel-network graphene foams. *J. Mater. Chem. A* **2014**, *2*, 16786–16792. [\[CrossRef\]](#)
63. Shunxin, J. A Simple Solution-Based Method to Prepare Honeycomb-Like Li₂S/Graphene Composite for Lithium-Sulfur Batteries. *Int. J. Electrochem. Sci.* **2018**, *13*, 3407–3419. [\[CrossRef\]](#)
64. Moura, D.; Pereira, R.F.; Gonçalves, I.C. Recent advances on bioprinting of hydrogels containing carbon materials. *Mater. Today Chem.* **2022**, *23*, 100617. [\[CrossRef\]](#)
65. Sha, J.; Li, Y.; Salvatierra, R.V.; Wang, T.; Dong, P.; Ji, Y.; Lee, S.-K.; Zhang, C.; Zhang, J.; Smith, R.H.; et al. Three-Dimensional Printed Graphene Foams. *ACS Nano* **2017**, *11*, 6860–6867. [\[CrossRef\]](#) [\[PubMed\]](#)
66. Tang, X.; Zhou, H.; Cai, Z.; Cheng, D.; He, P.; Xie, P.; Zhang, D.; Fan, T. Generalized 3D Printing of Graphene-Based Mixed-Dimensional Hybrid Aerogels. *ACS Nano* **2018**, *12*, 3502–3511. [\[CrossRef\]](#)
67. Yu, Z.-Y.; Chen, L.-F.; Song, L.-T.; Zhu, Y.-W.; Ji, H.-X.; Yu, S.-H. Free-standing boron and oxygen co-doped carbon nanofiber films for large volumetric capacitance and high rate capability supercapacitors. *Nano Energy* **2015**, *15*, 235–243. [\[CrossRef\]](#)
68. Bai, X.-L.; Gao, Y.-L.; Gao, Z.-Y.; Ma, J.-Y.; Tong, X.-L.; Sun, H.-B.; Wang, J.A. Supercapacitor performance of 3D-graphene/MnO₂ foam synthesized via the combination of chemical vapor deposition with hydrothermal method. *Appl. Phys. Lett.* **2020**, *117*, 183901. [\[CrossRef\]](#)
69. Li, J.; Yang, S.; Jiao, P.; Peng, Q.; Yin, W.; Yuan, Y.; Lu, H.; He, X.; Li, Y. Three-dimensional macroassembly of hybrid C@CoFe nanoparticles/reduced graphene oxide nanosheets towards multifunctional foam. *Carbon* **2020**, *157*, 427–436. [\[CrossRef\]](#)
70. Liu, W.; Cai, J.; Li, Z. Self-Assembly of Semiconductor Nanoparticles/Reduced Graphene Oxide (RGO) Composite Aerogels for Enhanced Photocatalytic Performance and Facile Recycling in Aqueous Photocatalysis. *ACS Sustain. Chem. Eng.* **2015**, *3*, 277–282. [\[CrossRef\]](#)
71. Zhang, M.; Song, Z.; Liu, H.; Wang, A.; Shao, S. MoO₂ coated few layers of MoS₂ and FeS₂ nanoflower decorated S-doped graphene interoverlapped network for high-energy asymmetric supercapacitor. *J. Colloid Interface Sci.* **2021**, *584*, 418–428. [\[CrossRef\]](#) [\[PubMed\]](#)
72. Park, S.; An, J.; Potts, J.R.; Velamakanni, A.; Murali, S.; Ruoff, R.S. Hydrazine-reduction of graphite- and graphene oxide. *Carbon* **2011**, *49*, 3019–3023. [\[CrossRef\]](#)
73. Yan, L.; Zhou, M.; Pang, X.; Gao, K. One-Step in Situ Synthesis of Reduced Graphene Oxide/Zn–Al Layered Double Hydroxide Film for Enhanced Corrosion Protection of Magnesium Alloys. *Langmuir* **2019**, *35*, 6312–6320. [\[CrossRef\]](#)
74. Shandilya, P.; Mittal, D.; Sudhaik, A.; Soni, M.; Raizada, P.; Saini, A.; Singh, P. GdVO₄ modified fluorine doped graphene nanosheets as dispersed photocatalyst for mitigation of phenolic compounds in aqueous environment and bacterial disinfection. *Sep. Purif. Technol.* **2019**, *210*, 804–816. [\[CrossRef\]](#)
75. Santos, F.C.U.; Paim, L.L.; da Silva, J.L.; Stradiotto, N.R. Electrochemical determination of total reducing sugars from bioethanol production using glassy carbon electrode modified with graphene oxide containing copper nanoparticles. *Fuel* **2016**, *163*, 112–121. [\[CrossRef\]](#)
76. Chen, W.; Li, S.; Chen, C.; Yan, L. Self-Assembly and Embedding of Nanoparticles by In Situ Reduced Graphene for Preparation of a 3D Graphene/Nanoparticle Aerogel. *Adv. Mater.* **2011**, *23*, 5679–5683. [\[CrossRef\]](#) [\[PubMed\]](#)
77. Kabtamu, D.M.; Chang, Y.-C.; Lin, G.-Y.; Bayeh, A.W.; Chen, J.-Y.; Wondimu, T.H.; Wang, C.-H. Three-dimensional annealed WO₃ nanowire/graphene foam as an electrocatalytic material for all vanadium redox flow batteries. *Sustain. Energy Fuels* **2017**, *1*, 2091–2100. [\[CrossRef\]](#)
78. Cai, L.; Lin, Z.; Wang, M.; Pan, F.; Chen, J.; Wang, Y.; Shen, X.; Chai, Y. Improved interfacial H₂O supply by surface hydroxyl groups for enhanced alkaline hydrogen evolution. *J. Mater. Chem. A* **2017**, *5*, 24091–24097. [\[CrossRef\]](#)
79. Worsley, M.A.; Pauzuskie, P.J.; Olson, T.Y.; Biener, J.; Satcher, J.J.H.; Baumann, T.F. Synthesis of Graphene Aerogel with High Electrical Conductivity. *J. Am. Chem. Soc.* **2010**, *132*, 14067–14069. [\[CrossRef\]](#)
80. Zhang, L.; Li, H.; Lai, X.; Wu, W.; Zeng, X. Hindered phenol functionalized graphene oxide for natural rubber. *Mater. Lett.* **2018**, *210*, 239–242. [\[CrossRef\]](#)
81. Bustos-Ramírez, K.; Martínez-Hernández, A.L.; Martínez-Barrera, G.; De Icaza, M.; Castaño, V.M.; Velasco-Santos, C. Covalently Bonded Chitosan on Graphene Oxide via Redox Reaction. *Materials* **2013**, *6*, 911–926. [\[CrossRef\]](#)
82. To, J.W.F.; Chen, Z.; Yao, H.; He, J.; Kim, K.; Chou, H.-H.; Pan, L.; Wilcox, J.; Cui, Y.; Bao, Z. Ultrahigh Surface Area Three-Dimensional Porous Graphitic Carbon from Conjugated Polymeric Molecular Framework. *ACS Central Sci.* **2015**, *1*, 68–76. [\[CrossRef\]](#) [\[PubMed\]](#)
83. Fang, B.; Chang, D.; Xu, Z.; Gao, C. A Review on Graphene Fibers: Expectations, Advances, and Prospects. *Adv. Mater.* **2020**, *32*, e1902664. [\[CrossRef\]](#) [\[PubMed\]](#)
84. Hummers, W.S., Jr.; Offeman, R.E. Preparation of Graphitic Oxide. *J. Am. Chem. Soc.* **1958**, *80*, 1339. [\[CrossRef\]](#)
85. Lawal, A.T. Graphene-based nano composites and their applications. A review. *Biosens. Bioelectron.* **2019**, *141*, 111384. [\[CrossRef\]](#) [\[PubMed\]](#)

86. Zhao, W.; Liu, H.; Meng, N.; Jian, M.; Wang, H.; Zhang, X. Graphene oxide incorporated thin film nanocomposite membrane at low concentration monomers. *J. Membr. Sci.* **2018**, *565*, 380–389. [\[CrossRef\]](#)
87. Akyüz, D.; Koca, A. Photocatalytic hydrogen production with reduced graphene oxide (RGO)-CdZnS nano-composites synthesized by solvothermal decomposition of dimethyl sulfoxide as the sulfur source. *J. Photochem. Photobiol. A Chem.* **2018**, *364*, 625–634. [\[CrossRef\]](#)
88. Kumar, N.; Rodriguez, J.R.; Pol, V.G.; Sen, A. Facile synthesis of 2D graphene oxide sheet enveloping ultrafine 1D LiMn_2O_4 as interconnected framework to enhance cathodic property for Li-ion battery. *Appl. Surf. Sci.* **2019**, *463*, 132–140. [\[CrossRef\]](#)
89. Aghazadeh, M. One-step electrophoretic/electrochemical synthesis of reduced graphene oxide/manganese oxide (RGO- Mn_3O_4) nanocomposite and study of its capacitive performance. *Anal. Bioanal. Electrochem.* **2018**, *10*, 961–973.
90. Jasmi, F.; Azeman, N.H.; Bakar, A.A.A.; Zan, M.S.D.; Badri, K.H.; Su'Ait, M.S. Ionic Conductive Polyurethane-Graphene Nanocomposite for Performance Enhancement of Optical Fiber Bragg Grating Temperature Sensor. *IEEE Access* **2018**, *6*, 47355–47363. [\[CrossRef\]](#)
91. Novoselov, K.S.; Geim, A.K.; Morozov, S.V.; Jiang, D.; Zhang, Y.; Dubonos, S.V.; Grigorieva, I.V.; Firsov, A.A. Electric Field Effect in Atomically Thin Carbon Films Supplementary. *Science* **2004**, *5*, 105–110. [\[CrossRef\]](#)
92. Qiu, B.; Li, Q.; Shen, B.; Xing, M.; Zhang, J. Stöber-like method to synthesize ultradispersed Fe_3O_4 nanoparticles on graphene with excellent Photo-Fenton reaction and high-performance lithium storage. *Appl. Catal. B Environ.* **2016**, *183*, 216–223. [\[CrossRef\]](#)
93. Wang, Y.; Zheng, Y.; Xu, X.; Dubuisson, E.; Bao, Q.; Lu, J.; Loh, K.P. Electrochemical Delamination of CVD-Grown Graphene Film: Toward the Recyclable Use of Copper Catalyst. *ACS Nano* **2011**, *5*, 9927–9933. [\[CrossRef\]](#) [\[PubMed\]](#)
94. Geim, A.K.; Novoselov, K.S. The rise of graphene. *Nat. Mater.* **2007**, *6*, 183–191. [\[CrossRef\]](#) [\[PubMed\]](#)
95. Dong, Z.; Jiang, C.; Cheng, H.; Zhao, Y.; Shi, G.; Jiang, L.; Qu, L. Facile Fabrication of Light, Flexible and Multifunctional Graphene Fibers. *Adv. Mater.* **2012**, *24*, 1856–1861. [\[CrossRef\]](#) [\[PubMed\]](#)
96. Kim, K.S.; Zhao, Y.; Jang, H.; Lee, S.Y.; Kim, J.M.; Kim, K.S.; Ahn, J.-H.; Kim, P.; Choi, J.-Y.; Hong, B.H. Large-scale pattern growth of graphene films for stretchable transparent electrodes. *Nature* **2009**, *457*, 706–710. [\[CrossRef\]](#) [\[PubMed\]](#)
97. Qiu, B.; Deng, Y.; Du, M.; Xing, M.; Zhang, J. Ultradispersed Cobalt Ferrite Nanoparticles Assembled in Graphene Aerogel for Continuous Photo-Fenton Reaction and Enhanced Lithium Storage Performance. *Sci. Rep.* **2016**, *6*, 29099. [\[CrossRef\]](#) [\[PubMed\]](#)
98. Chen, S.; Duan, J.; Ran, J.; Jaroniec, M.; Qiao, S.Z. N-doped graphene film-confined nickel nanoparticles as a highly efficient three-dimensional oxygen evolution electrocatalyst. *Energy Environ. Sci.* **2013**, *6*, 3693–3699. [\[CrossRef\]](#)
99. Shen, Y.; Fang, Q.; Chen, B. Environmental Applications of Three-Dimensional Graphene-Based Macrostructures: Adsorption, Transformation, and Detection. *Environ. Sci. Technol.* **2015**, *49*, 67–84. [\[CrossRef\]](#)
100. Qiu, B.; Deng, Y.; Li, Q.; Shen, B.; Xing, M.; Zhang, J. Rational Design of a Unique Ternary Structure for Highly Photocatalytic Nitrobenzene Reduction. *J. Phys. Chem. C* **2016**, *120*, 12125–12131. [\[CrossRef\]](#)
101. Bolver, C.; Bedia, J.; Gómez-Avilés, A.; Peñas-Garzón, M.; Rodriguez, J.J. Semiconductor Photocatalysis for Water Purification. *Nanoscale Mater. Water Purif.* **2018**, *22*, 581–651.
102. Zhang, M.; Luo, W.; Wei, Z.; Jiang, W.; Liu, D.; Zhu, Y. Separation free $\text{C}_3\text{N}_4/\text{SiO}_2$ hybrid hydrogels as high active photocatalysts for TOC removal. *Appl. Catal. B Environ.* **2016**, *194*, 105–110. [\[CrossRef\]](#)
103. Qiu, B.; Xing, M.; Zhang, J. Mesoporous TiO_2 Nanocrystals Grown in Situ on Graphene Aerogels for High Photocatalysis and Lithium-Ion Batteries. *J. Am. Chem. Soc.* **2014**, *136*, 5852–5855. [\[CrossRef\]](#) [\[PubMed\]](#)
104. Fan, Y.; Ma, W.; Han, D.; Gan, S.; Dong, X.; Niu, L. Convenient Recycling of 3D AgX /Graphene Aerogels ($\text{X} = \text{Br}, \text{Cl}$) for Efficient Photocatalytic Degradation of Water Pollutants. *Adv. Mater.* **2015**, *27*, 3767–3773. [\[CrossRef\]](#) [\[PubMed\]](#)
105. Iijima, S. Helical microtubules of graphitic carbon. *Nature* **1991**, *354*, 56–58. [\[CrossRef\]](#)
106. Sun, D.; Hong, R.; Liu, J.; Wang, F.; Wang, Y. Preparation of carbon nanomaterials using two-group arc discharge plasma. *Chem. Eng. J.* **2016**, *303*, 217–230. [\[CrossRef\]](#)
107. Zhao, X.; Zhao, T.; Peng, X.; Hu, J.; Yang, W. Catalyst effect on the preparation of single-walled carbon nanotubes by a modified arc discharge. *Full-Nanotub. Carbon Nanostruct.* **2019**, *27*, 52–57. [\[CrossRef\]](#)
108. Tepale-Cortés, A.; Moreno-Saavedra, H.; Hernández-Tenorio, C.; Rojas-Ramírez, T.; Illescas, J. Multi-walled Carbon Nanotubes Synthesis by Arc Discharge Method in a Glass Chamber. *J. Mex. Chem. Soc.* **2021**, *65*, 480–490. [\[CrossRef\]](#)
109. Smalley, R.E. Discovering the Fullerenes (Nobel Lecture). *Angew. Chem. (Int. Ed. Engl.)* **1997**, *36*, 1594–1601. [\[CrossRef\]](#)
110. Khashan, K.S.; Sulaiman, G.; Mahdi, R. Preparation of iron oxide nanoparticles-decorated carbon nanotube using laser ablation in liquid and their antimicrobial activity. *Artif. Cells Nanomed. Biotechnol.* **2017**, *45*, 1699–1709. [\[CrossRef\]](#)
111. Wu, X.; Yin, H.; Li, Q. Ablation and Patterning of Carbon Nanotube Film by Femtosecond Laser Irradiation. *Appl. Sci.* **2019**, *9*, 3045. [\[CrossRef\]](#)
112. Mostafa, A.M.; Mwafy, E.A.; Toghan, A. ZnO nanoparticles decorated carbon nanotubes via pulsed laser ablation method for degradation of methylene blue dyes. *Colloids Surfaces A Physicochem. Eng. Asp.* **2021**, *627*, 127204. [\[CrossRef\]](#)
113. Jourdain, V.; Bichara, C. Current understanding of the growth of carbon nanotubes in catalytic chemical vapour deposition. *Carbon* **2013**, *58*, 2–39. [\[CrossRef\]](#)
114. Razak, S.A.; Nordin, N.N.; Sulaiman, M.A.; Yusoff, M.; Masri, M.N. A Brief Review on Recent Development of Carbon Nanotubes by Chemical Vapor Deposition. *J. Trop. Resour. Sustain. Sci.* **2021**, *4*, 68–71. [\[CrossRef\]](#)
115. Gspann, T.S.; Juckes, S.M.; Niven, J.F.; Johnson, M.B.; Elliott, J.A.; White, M.A.; Windle, A.H. High thermal conductivities of carbon nanotube films and micro-fibres and their dependence on morphology. *Carbon* **2017**, *114*, 160–168. [\[CrossRef\]](#)

116. Duc Vu Quyen, N.; Khieu, D.Q.; Tuyen, T.N.; Tin, D.X.; Thi Hoang Diem, B. Carbon Nanotubes: Synthesis via Chemical Vapour Deposition without Hydrogen, Surface Modification, and Application. *J. Chem.* **2019**, *2019*, 4260153. [\[CrossRef\]](#)
117. McLean, B.; Kauppinen, E.I.; Page, A.J. Initial competing chemical pathways during floating catalyst chemical vapor deposition carbon nanotube growth. *J. Appl. Phys.* **2021**, *129*, 044302. [\[CrossRef\]](#)
118. Zhao, N.; Wu, Q.; Zhang, X.; Yang, T.; Li, D.; Zhang, X.; Ma, C.; Liu, R.; Xin, L.; He, M. Chemical vapor deposition growth of single-walled carbon nanotubes from plastic polymers. *Carbon* **2022**, *187*, 29–34. [\[CrossRef\]](#)
119. Asinovsky, E.I.; Amirov, R.H.; Isakaev, E.K.; Kiselev, V.I. Thermal plasma torch for synthesis of carbon nanotubes. *High Temp. Mater. Process.* **2006**, *10*, 197–206. [\[CrossRef\]](#)
120. Hong, Y.C.; Uhm, H.S. Production of carbon nanotubes by microwave plasma torch at atmospheric pressure. *Phys. Plasmas* **2005**, *12*, 053504. [\[CrossRef\]](#)
121. Amirov, R.H.; Isakaev, E.K.; Shavelkina, M.B.; Shatalova, T. Synthesis of carbon nanotubes by high current divergent anode-channel plasma torch. *J. Phys. Conf. Ser.* **2014**, *550*, 012023. [\[CrossRef\]](#)
122. Bodnaryk, W.J.; Fong, D.; Adronov, A. Enrichment of Metallic Carbon Nanotubes Using a Two-Polymer Extraction Method. *ACS Omega* **2018**, *3*, 16238–16245. [\[CrossRef\]](#)
123. Aïssa, B.; Ali, A.; Bentouaf, A.; Khan, W.; Zakaria, Y.; Mahmoud, K.A.; Ali, K.; Muhammad, N.M.; Mansour, S.A. Influence of single-walled carbon nanotubes induced exciton dissociation improvement on hybrid organic photovoltaic devices. *J. Appl. Phys.* **2019**, *126*, 113101. [\[CrossRef\]](#)
124. Gotthardt, J.M.; Schneider, S.; Brohmann, M.; Leingang, S.; Sauter, E.; Zharnikov, M.; Himmel, H.-J.; Zaumseil, J. Molecular n-Doping of Large- and Small-Diameter Carbon Nanotube Field-Effect Transistors with Tetrakis(tetramethylguanidino)benzene. *ACS Appl. Electron. Mater.* **2021**, *3*, 804–812. [\[CrossRef\]](#)
125. Ajayan, P.M.; Ebbesen, T.W. Nanometre-size tubes of carbon. *Rep. Prog. Phys.* **1997**, *60*, 1025–1062. [\[CrossRef\]](#)
126. Ruoff, R.S.; Lorents, D.C. Mechanical and thermal properties of carbon nanotubes. *Carbon* **1995**, *33*, 925–930. [\[CrossRef\]](#)
127. Dong, X.; Zhang, H.-B.; Lin, G.-D.; Yuan, Y.-Z.; Tsai, K. Highly Active CNT-Promoted Cu–ZnO–Al₂O₃ Catalyst for Methanol Synthesis from H₂/CO/CO₂. *Catal. Lett.* **2003**, *85*, 237–246. [\[CrossRef\]](#)
128. Huang, J.; Zhang, Q.; Zhao, M.; Wei, F. A review of the large-scale production of carbon nanotubes: The practice of nanoscale process engineering. *Chin. Sci. Bull.* **2012**, *57*, 157–166. [\[CrossRef\]](#)
129. Schnorr, J.M.; Swager, T.M. Emerging Applications of Carbon Nanotubes. *Chem. Mater.* **2011**, *23*, 646–657. [\[CrossRef\]](#)
130. Zhang, Q.; Zuo, Y.-Z.; Han, M.-H.; Wang, J.-F.; Jin, Y.; Wei, F. Long carbon nanotubes intercrossed Cu/Zn/Al/Zr catalyst for CO/CO₂ hydrogenation to methanol/dimethyl ether. *Catal. Today* **2010**, *150*, 55–60. [\[CrossRef\]](#)
131. Ozden, S.; Tiwary, C.S.; Hart, A.H.C.; Chipara, A.C.; Romero-Aburto, R.; Rodrigues, M.-T.F.; Taha-Tijerina, J.; Vajtai, R.; Ajayan, P.M. Density Variant Carbon Nanotube Interconnected Solids. *Adv. Mater.* **2015**, *27*, 1842–1850. [\[CrossRef\]](#)
132. Ozden, S.; Narayanan, T.N.; Tiwary, C.S.; Dong, P.; Hart, A.H.C.; Vajtai, R.; Ajayan, P.M. 3D Macroporous Solids from Chemically Cross-linked Carbon Nanotubes. *Small* **2015**, *11*, 688–693. [\[CrossRef\]](#) [\[PubMed\]](#)
133. Guiderdoni, C.; Estournes, C.; Peigney, A.; Weibel, A.; Turq, V.; Laurent, C. The preparation of double-walled carbon nanotube/Cu composites by spark plasma sintering, and their hardness and friction properties. *Carbon* **2011**, *49*, 4535–4543. [\[CrossRef\]](#)
134. Ozden, S.; Brunetto, G.; Karthiselva, N.S.; Galvão, D.S.; Roy, A.; Bakshi, S.R.; Tiwary, C.S.; Ajayan, P.M. Controlled 3D Carbon Nanotube Structures by Plasma Welding. *Adv. Mater. Interfaces* **2016**, *3*, 1500755. [\[CrossRef\]](#)
135. Al-Hakami, S.M.; Khalil, A.B.; Laoui, T.; Atieh, M.A. Fast Disinfection of *Escherichia coli* Bacteria Using Carbon Nanotubes Interaction with Microwave Radiation. *Bioinorg. Chem. Appl.* **2013**, *2013*, 458943. [\[CrossRef\]](#) [\[PubMed\]](#)
136. Khalid, N.; Majid, A.; Tahir, M.B.; Niaz, N.; Khalid, S. Carbonaceous-TiO₂ nanomaterials for photocatalytic degradation of pollutants: A review. *Ceram. Int.* **2017**, *43*, 14552–14571. [\[CrossRef\]](#)
137. Chen, M.-L.; Zhang, F.-J.; Oh, W.-C. Synthesis, characterization, and photocatalytic analysis of CNT/TiO₂ composites derived from MWCNTs and titanium sources. *New Carbon Mater.* **2009**, *24*, 159–166. [\[CrossRef\]](#)
138. Jauris, I.M.; Fagan, S.B.; Adebayo, M.A.; Machado, F.M. Adsorption of acridine orange and methylene blue synthetic dyes and anthracene on single wall carbon nanotubes: A first principle approach. *Comput. Theor. Chem.* **2016**, *1076*, 42–50. [\[CrossRef\]](#)
139. Zhang, W.; Li, G.; Liu, H.; Chen, J.; Ma, S.; An, T. Micro/nano-bubble assisted synthesis of Au/TiO₂@CNTs composite photocatalyst for photocatalytic degradation of gaseous styrene and its enhanced catalytic mechanism. *Environ. Sci. Nano* **2019**, *6*, 948–958. [\[CrossRef\]](#)
140. Wang, W.; Wang, S.; Ma, X.; Gong, J. Recent advances in catalytic hydrogenation of carbon dioxide. *Chem. Soc. Rev.* **2011**, *40*, 3703–3727. [\[CrossRef\]](#)
141. Wang, D.; Xie, Z.; Porosoff, M.D.; Chen, J.G. Recent advances in carbon dioxide hydrogenation to produce olefins and aromatics. *Chem* **2021**, *7*, 2277–2311. [\[CrossRef\]](#)
142. Duyar, M.; Ramachandran, A.; Wang, C.; Farrauto, R.J. Kinetics of CO₂ methanation over Ru/ γ -Al₂O₃ and implications for renewable energy storage applications. *J. CO₂ Util.* **2015**, *12*, 27–33. [\[CrossRef\]](#)
143. Mutz, B.; Carvalho, H.W.; Mangold, S.; Kleist, W.; Grunwaldt, J.-D. Methanation of CO₂: Structural response of a Ni-based catalyst under fluctuating reaction conditions unraveled by operando spectroscopy. *J. Catal.* **2015**, *327*, 48–53. [\[CrossRef\]](#)
144. Younas, M.; Kong, L.L.; Bashir, M.J.K.; Nadeem, H.; Shehzad, A.; Sethupathi, S. Recent Advancements, Fundamental Challenges, and Opportunities in Catalytic Methanation of CO₂. *Energy Fuels* **2016**, *30*, 8815–8831. [\[CrossRef\]](#)

145. Rönsch, S.; Schneider, J.; Matthischke, S.; Schlüter, M.; Götz, M.; Lefebvre, J.; Prabhakaran, P.; Bajohr, S. Review on methanation—From fundamentals to current projects. *Fuel* **2016**, *166*, 276–296. [\[CrossRef\]](#)
146. Potocnik, P. *Natural Gas*; BoD—Books on Demand; IntechOpen: London, UK, 2010.
147. Thampi, K.R.; Kiwi, J.; Grätzel, M. Methanation and photo-methanation of carbon dioxide at room temperature and atmospheric pressure. *Nature* **1987**, *327*, 506–508. [\[CrossRef\]](#)
148. Koschany, F.; Schlereth, D.; Hinrichsen, O. On the kinetics of the methanation of carbon dioxide on coprecipitated NiAl(O)_x. *Appl. Catal. B Environ.* **2016**, *181*, 504–516. [\[CrossRef\]](#)
149. Fujiwara, M.; Satake, T.; Shiokawa, K.; Sakurai, H. CO₂ hydrogenation for C₂₊ hydrocarbon synthesis over composite catalyst using surface modified HB zeolite. *Appl. Catal. B Environ.* **2015**, *179*, 37–43. [\[CrossRef\]](#)
150. Zhang, J.; Qian, Q.; Cui, M.; Chen, C.; Liu, S.; Han, B. Synthesis of ethanol from paraformaldehyde, CO₂ and H₂. *Green Chem.* **2017**, *19*, 4396–4401. [\[CrossRef\]](#)
151. Le Duff, C.S.; Lawrence, M.J.; Rodriguez, P. Role of the Adsorbed Oxygen Species in the Selective Electrochemical Reduction of CO₂ to Alcohols and Carbonyls on Copper Electrodes. *Angew. Chem.* **2017**, *129*, 13099–13104. [\[CrossRef\]](#)
152. Climent, V.; Feliu, J.M. Cyclic Voltammetry. In *Encyclopedia of Interfacial Chemistry: Surface Science and Electrochemistry*; Elsevier: Amsterdam, The Netherlands, 2018; pp. 48–74.
153. Ezenarro, J.J.; Párraga-Niño, N.; Sabrià, M.; Del Campo, F.; Muñoz-Pascual, F.-X.; Mas, J.; Uria, N. Rapid Detection of *Legionella pneumophila* in Drinking Water, Based on Filter Immunoassay and Chronoamperometric Measurement. *Biosensors* **2020**, *10*, 102. [\[CrossRef\]](#)
154. Ali, A.; Oh, W.-C. Preparation of Nanowire like WSe₂-Graphene Nanocomposite for Photocatalytic Reduction of CO₂ into CH₃OH with the Presence of Sacrificial Agents. *Sci. Rep.* **2017**, *7*, 1867. [\[CrossRef\]](#) [\[PubMed\]](#)
155. Biswas, R.U.D.; Ali, A.; Cho, K.Y.; Oh, W.-C. Novel synthesis of WSe₂-Graphene-TiO₂ ternary nanocomposite via ultrasonic technics for high photocatalytic reduction of CO₂ into CH₃OH. *Ultrason. Sonochem.* **2018**, *42*, 738–746. [\[CrossRef\]](#)
156. Dinh, C.-T.; Burdyny, T.; Kibria, M.G.; Seifitokaldani, A.; Gabardo, C.M.; de Arquer, F.P.G.; Kiani, A.; Edwards, J.P.; De Luna, P.; Bushuyev, O.S.; et al. CO₂ electroreduction to ethylene via hydroxide-mediated copper catalysis at an abrupt interface. *Science* **2018**, *360*, 783–787. [\[CrossRef\]](#) [\[PubMed\]](#)
157. Ma, Z.; Porosoff, M.D. Development of Tandem Catalysts for CO₂ Hydrogenation to Olefins. *ACS Catal.* **2019**, *9*, 2639–2656. [\[CrossRef\]](#)
158. Huan, T.N.; Corte, D.A.D.; Lamaison, S.; Karapinar, D.; Lutz, L.; Menguy, N.; Foldyna, M.; Turren-Cruz, S.-H.; Hagfeldt, A.; Bella, F.; et al. Low-cost high-efficiency system for solar-driven conversion of CO₂ to hydrocarbons. *Proc. Natl. Acad. Sci. USA* **2019**, *116*, 9735–9740. [\[CrossRef\]](#) [\[PubMed\]](#)
159. Wu, Y.; Jiang, Z.; Lu, X.; Liang, Y.; Wang, H. Domino electroreduction of CO₂ to methanol on a molecular catalyst. *Nature* **2019**, *575*, 639–642. [\[CrossRef\]](#)
160. Ramirez, A.; Ould-Chikh, S.; Gevers, L.; Chowdhury, A.D.; Abou-Hamad, E.; Aguilar-Tapia, A.; Hazemann, J.; Wehbe, N.; Al Abdulghani, A.J.; Kozlov, S.M.; et al. Tandem Conversion of CO₂ to Valuable Hydrocarbons in Highly Concentrated Potassium Iron Catalysts. *Chemcatchem* **2019**, *11*, 2879–2886. [\[CrossRef\]](#)
161. Tada, S.; Otsuka, F.; Fujiwara, K.; Moularas, C.; Deligiannakis, Y.; Kinoshita, Y.; Uchida, S.; Honma, T.; Nishijima, M.; Kikuchi, R. Development of CO₂-to-Methanol Hydrogenation Catalyst by Focusing on the Coordination Structure of the Cu Species in Spinel-Type Oxide Mg_{1-x}Cu_xAl₂O₄. *ACS Catal.* **2020**, *10*, 15186–15194. [\[CrossRef\]](#)
162. Tada, S.; Kinoshita, H.; Ochiai, N.; Chokkalingam, A.; Hu, P.; Yamauchi, N.; Kobayashi, Y.; Iyoki, K. Search for solid acid catalysts aiming at the development of bifunctional tandem catalysts for the one-pass synthesis of lower olefins via CO₂ hydrogenation. *Int. J. Hydrogen Energy* **2021**, *46*, 36721–36730. [\[CrossRef\]](#)
163. Rahmani, A.; Aubert, X.; Fagnon, N.; Nikravech, M. Liquid oxygenated hydrocarbons produced during reforming of CH₄ and CO₂ in a surface dielectric barrier discharge: Effects of steam on conversion and products distribution. *J. Appl. Phys.* **2021**, *129*, 193304. [\[CrossRef\]](#)
164. Islam, H.; Burheim, O.S.; Hihn, J.-Y.; Pollet, B. Sonochemical conversion of CO₂ into hydrocarbons: The Sabatier reaction at ambient conditions. *Ultrason. Sonochem.* **2021**, *73*, 105474. [\[CrossRef\]](#) [\[PubMed\]](#)
165. Tian, G.; Wu, Y.; Wu, S.; Huang, S.; Gao, J. Influence of Mn and Mg oxides on the performance of In₂O₃ catalysts for CO₂ hydrogenation to methanol. *Chem. Phys. Lett.* **2022**, *786*, 139173. [\[CrossRef\]](#)
166. Chernyak, S.A.; Kustov, A.L.; Stolbov, D.N.; Tedeeva, M.A.; Isaikina, O.Y.; Maslakov, K.I.; Usol'tseva, N.V.; Savilov, S.V. Chromium catalysts supported on carbon nanotubes and graphene nanoflakes for CO₂-assisted oxidative dehydrogenation of propane. *Appl. Surf. Sci.* **2022**, *578*, 152099. [\[CrossRef\]](#)
167. Davis, B.H. Fischer–Tropsch synthesis: Current mechanism and futuristic needs. *Fuel Process. Technol.* **2001**, *71*, 157–166. [\[CrossRef\]](#)
168. Wang, H.; Li, J. Microporous Metal–Organic Frameworks for Adsorptive Separation of C₅–C₆ Alkane Isomers. *Acc. Chem. Res.* **2019**, *52*, 1968–1978. [\[CrossRef\]](#)
169. Golubev, K.; Batova, T.; Kolesnichenko, N.; Maximov, A. Synthesis of C₂–C₄ olefins from methanol as a product of methane partial oxidation over zeolite catalyst. *Catal. Commun.* **2019**, *129*, 105744. [\[CrossRef\]](#)
170. Zhang, Z.; Liu, Y.; Jia, L.; Sun, C.; Chen, B.; Liu, R.; Tan, Y.; Tu, W. Effects of the reducing gas atmosphere on performance of FeCeNa catalyst for the hydrogenation of CO₂ to olefins. *Chem. Eng. J.* **2022**, *428*, 131388. [\[CrossRef\]](#)

171. Saeidi, S.; Amin, N.A.S.; Rahimpour, M.R. Hydrogenation of CO₂ to value-added products—A review and potential future developments. *J. CO₂ Util.* **2014**, *5*, 66–81. [\[CrossRef\]](#)
172. Aziz, M.A.A.; Jalil, A.A.; Triwahyono, S.; Ahmad, A. CO₂ methanation over heterogeneous catalysts: Recent progress and future prospects. *Green Chem.* **2015**, *17*, 2647–2663. [\[CrossRef\]](#)
173. Reimer, J.; Müller, S.; De Boni, E.; Vogel, F. Hydrogen-enhanced catalytic hydrothermal gasification of biomass. *Biomass-Convert. Biorefinery* **2017**, *7*, 511–519. [\[CrossRef\]](#)
174. Navarro-Jaén, S.; Navarro, J.C.; Bobadilla, L.F.; Centeno, M.A.; Laguna, O.H.; Odriozola, J.A. Size-tailored Ru nanoparticles deposited over γ -Al₂O₃ for the CO₂ methanation reaction. *Appl. Surf. Sci.* **2019**, *483*, 750–761. [\[CrossRef\]](#)
175. Jin, S.; Hao, Z.; Zhang, K.; Yan, Z.; Chen, J. Advances and Challenges for the Electrochemical Reduction of CO₂ to CO: From Fundamentals to Industrialization. *Angew. Chem. Int. Ed.* **2021**, *60*, 20627–20648. [\[CrossRef\]](#) [\[PubMed\]](#)
176. Fu, S.; Angelidaki, I.; Zhang, Y. In situ Biogas Upgrading by CO₂-to-CH₄ Bioconversion. *Trends Biotechnol.* **2021**, *39*, 336–347. [\[CrossRef\]](#) [\[PubMed\]](#)
177. Miletto, I.; Catizzzone, E.; Bonura, G.; Ivaldi, C.; Migliori, M.; Gianotti, E.; Marchese, L.; Frusteri, F.; Giordano, G. In Situ FT-IR Characterization of CuZnZr/Ferrierite Hybrid Catalysts for One-Pot CO₂-to-DME Conversion. *Materials* **2018**, *11*, 2275. [\[CrossRef\]](#)
178. Boreriboon, N.; Jiang, X.; Song, C.; Prasassarakich, P. Higher Hydrocarbons Synthesis from CO₂ Hydrogenation over K- and La-Promoted Fe-Cu/TiO₂ Catalysts. *Top. Catal.* **2018**, *61*, 1551–1562. [\[CrossRef\]](#)
179. Liu, M.; Yi, Y.; Wang, L.; Guo, H.; Bogaerts, A. Hydrogenation of Carbon Dioxide to Value-Added Plasma Catalysis. *Catalysts* **2019**, *9*, 275. [\[CrossRef\]](#)
180. Ahmad, K.N.; Anuar, S.A.; Isahak, W.N.R.W.; Rosli, M.I.; Yarmo, M.A. Influences of calcination atmosphere on nickel catalyst supported on mesoporous graphitic carbon nitride thin sheets for CO methanation. *ACS Appl. Mater. Interfaces* **2020**, *12*, 7102–7113. [\[CrossRef\]](#)
181. Ahmad, K.N.; Isahak, W.N.R.W.; Rosli, M.I.; Yusop, M.R.; Kassim, M.B.; Yarmo, M.A. Rare earth metal doped nickel catalysts supported on exfoliated graphitic carbon nitride for highly selective CO and CO₂ methanation. *Appl. Surf. Sci.* **2022**, *571*, 151321. [\[CrossRef\]](#)
182. Bahari, N.A.; Isahak, W.N.R.W.; Masdar, M.S.; Yaakob, Z. Clean hydrogen generation and storage strategies via CO₂ utilization into chemicals and fuels: A review. *Int. J. Energy Res.* **2020**, *43*, 5128–5150. [\[CrossRef\]](#)
183. Hasan, S.Z.; Ahmad, K.N.; Isahak, W.N.R.W.; Masdar, M.S.; Jahim, J.M. Synthesis of low-cost catalyst NiO (111) for CO₂ hydrogenation into short-chain carboxylic acids. *Int. J. Hydrog. Energy* **2020**, *45*, 22281–22290. [\[CrossRef\]](#)
184. Zhu, M.; Tian, P.; Cao, X.; Chen, J.; Pu, T.; Shi, B.; Xu, J.; Moon, J.; Wu, Z.; Han, Y.-F. Vacancy engineering of the nickel-based catalysts for enhanced CO₂ methanation. *Appl. Catal. B Environ.* **2021**, *282*, 119561. [\[CrossRef\]](#)
185. Gac, W.; Zawadzki, W.; Rotko, M.; Greluk, M.; Słowik, G.; Pennemann, H.; Neuberger, S.; Zapf, R.; Kolb, G. Direct Conversion of Carbon Dioxide to Methane over Ceria- and Alumina-Supported Nickel Catalysts for Biogas Valorization. *Chempluschem* **2021**, *86*, 889–903. [\[CrossRef\]](#) [\[PubMed\]](#)
186. Chang, Y.-B.; Zhang, C.; Lu, X.-L.; Zhang, W.; Lu, T.-B. Graphdiyne enables ultrafine Cu nanoparticles to selectively reduce CO₂ to C₂₊ products. *Nano Res.* **2022**, *15*, 195–201. [\[CrossRef\]](#)
187. Kattel, S.; Yan, B.; Yang, Y.; Chen, J.G.; Liu, P. Optimizing Binding Energies of Key Intermediates for CO₂ Hydrogenation to Methanol over Oxide-Supported Copper. *J. Am. Chem. Soc.* **2016**, *138*, 12440–12450. [\[CrossRef\]](#) [\[PubMed\]](#)
188. Kumari, N.; Haider, M.A.; Agarwal, M.; Sinha, N.; Basu, S. Role of Reduced CeO₂(110) Surface for CO₂ Reduction to CO and Methanol. *J. Phys. Chem. C* **2016**, *120*, 16626–16635. [\[CrossRef\]](#)
189. Cheng, Z.; Lo, C.S. Mechanistic and microkinetic analysis of CO₂ hydrogenation on ceria. *Phys. Chem. Chem. Phys.* **2016**, *18*, 7987–7996. [\[CrossRef\]](#)
190. Chai, G.-L.; Guo, Z.-X. Highly effective sites and selectivity of nitrogen-doped graphene/CNT catalysts for CO₂ electrochemical reduction. *Chem. Sci.* **2016**, *7*, 1268–1275. [\[CrossRef\]](#)
191. Zhang, W.; Ma, X.-L.; Xiao, H.; Lei, M.; Li, J. Mechanistic Investigations on Thermal Hydrogenation of CO₂ to Methanol by Nanostructured CeO₂(100): The Crystal-Plane Effect on Catalytic Reactivity. *J. Phys. Chem. C* **2019**, *123*, 11763–11771. [\[CrossRef\]](#)
192. Jiang, F.; Wang, S.; Liu, B.; Liu, J.; Wang, L.; Xiao, Y.; Xu, Y.; Liu, X. Insights into the Influence of CeO₂ Crystal Facet on CO₂ Hydrogenation to Methanol over Pd/CeO₂ Catalysts. *ACS Catal.* **2020**, *10*, 11493–11509. [\[CrossRef\]](#)
193. Coufourier, S.; Gaillard, Q.G.; Lohier, J.-F.; Poater, A.; Gaillard, S.; Renaud, J.-L. Hydrogenation of CO₂, Hydrogenocarbonate, and Carbonate to Formate in Water using Phosphine Free Bifunctional Iron Complexes. *ACS Catal.* **2020**, *10*, 2108–2116. [\[CrossRef\]](#)
194. Cao, A.; Wang, Z.; Li, H.; Elnabawy, A.O.; Nørskov, J.K. New insights on CO and CO₂ hydrogenation for methanol synthesis: The key role of adsorbate-adsorbate interactions on Cu and the highly active MgO-Cu interface. *J. Catal.* **2021**, *400*, 325–331. [\[CrossRef\]](#)
195. Rasteiro, L.F.; De Sousa, R.A.; Vieira, L.H.; Ocampo-Restrepo, V.K.; Verga, L.G.; Assaf, J.M.; Da Silva, J.L.; Assaf, E.M. Insights into the alloy-support synergistic effects for the CO₂ hydrogenation towards methanol on oxide-supported Ni₅Ga₃ catalysts: An experimental and DFT study. *Appl. Catal. B Environ.* **2022**, *302*, 120842. [\[CrossRef\]](#)
196. Kovalskii, A.M.; Volkov, I.N.; Evdokimenko, N.D.; Tkachenko, O.P.; Leybo, D.V.; Chepkasov, I.V.; Popov, Z.I.; Matveev, A.T.; Manakhov, A.; Permyakova, E.S.; et al. Hexagonal BN- and BNO-supported Au and Pt nanocatalysts in carbon monoxide oxidation and carbon dioxide hydrogenation reactions. *Appl. Catal. B Environ.* **2022**, *303*, 120891. [\[CrossRef\]](#)

197. Wang, Z.-Q.; Liu, H.-H.; Wu, X.-P.; Hu, P.; Gong, X.-Q. Hydride Generation on the Cu-Doped CeO₂(111) Surface and Its Role in CO₂ Hydrogenation Reactions. *Catalysts* **2022**, *12*, 963. [\[CrossRef\]](#)
198. Patel, J.; Parikh, S.; Patel, S.; Patel, R.; Patel, P. Carbon Nanotube (CNTs): Structure, Synthesis, Purification, Functionalisation, Pharmacology, Toxicology, Biodegradation and Application as Nanomedicine and Biosensor. *J. Pharm. Sci. Med. Res.* **2021**, *1*, 17–44. [\[CrossRef\]](#)
199. Saravanan, M.; Babu, S.; Sivaprasad, K.; Jagannatham, M. Techno-economics of carbon nanotubes produced by open air arc discharge method. *Int. J. Eng. Sci. Technol.* **2010**, *2*, 100–108. [\[CrossRef\]](#)
200. O'Byrne, J.P.; Owen, R.E.; Minett, D.R.; Pascu, S.I.; Plucinski, P.K.; Jones, M.D.; Mattia, D. High CO₂ and CO conversion to hydrocarbons using bridged Fe nanoparticles on carbon nanotubes. *Catal. Sci. Technol.* **2013**, *3*, 1202–1207. [\[CrossRef\]](#)
201. Serp, P.; Corrias, M.; Kalck, P. Carbon nanotubes and nanofibers in catalysis. *Appl. Catal. A Gen.* **2003**, *253*, 337–358. [\[CrossRef\]](#)

Disclaimer/Publisher's Note: The statements, opinions and data contained in all publications are solely those of the individual author(s) and contributor(s) and not of MDPI and/or the editor(s). MDPI and/or the editor(s) disclaim responsibility for any injury to people or property resulting from any ideas, methods, instructions or products referred to in the content.